Spatially resolved properties of the ionized gas in the H II galaxy J084220+115000

D. Fernández-Arenas,[1]⋆ E. Carrasco [ID],[1] R. Terlevich [ID],[1,2] E. Terlevich [ID],[1]† R. Amorín,[3,4] F. Bresolin [ID],[5]
R. Chávez,[6,7] A. L. González-Morán,[8,9] D. Rosa-González,[1] Y. D. Mayya,[1] O. Vega,[1]
J. Zaragoza-Cardiel [ID],[1,7] J. Méndez-Abreu,[8,9] R. Izazaga-Pérez,[1] A. Gil de Paz,[10,11] J. Gallego,[10,11]
J. Iglesias-Páramo,[12] M.L. García-Vargas,[13] P. Gómez-Alvarez,[13] A. Castillo-Morales,[10,11]
N. Cardiel [ID],[10,11] S. Pascual[10,11] and A. Pérez-Calpena[13]

[1]*Instituto Nacional de Astrofísica, Óptica y Electrónica, Tonantzintla, Puebla C.P. 72840, Mexico*
[2]*Institute of Astronomy, University of Cambridge, Cambridge CB3 0HA, UK*
[3]*Departamento de Astronomía, Universidad de La Serena, Av. Juan Cisternas 1200 Norte, La Serena, Chile*
[4]*Instituto de Investigación Multidisciplinar en Ciencia y Tecnología, Universidad de La Serena, Raúl Bitrán 1305, La Serena, Chile*
[5]*Institute for Astronomy, 2680 Woodlawn Drive, Honolulu, HI 96822, USA*
[6]*Instituto de Radioastronomía y Astrofísica, UNAM, Campus Morelia, C.P. 58089 Morelia, México*
[7]*Consejo Nacional de Ciencia y Tecnología, Av. Insurgentes Sur 1582, 03940 Mexico City, Mexico*
[8]*Instituto de Astrofísica de Canarias, C/ Vía Láctea s/n, 38205 La Laguna, Tenerife, Spain*
[9]*Departamento de Astrofísica, Universidad de La Laguna, E-38205 La Laguna, Tenerife, Spain.*
[10]*Departamento de Física de la Tierra y Astrofísica, Fac. CC. Físicas, Universidad Complutense de Madrid, Plaza de las Ciencias, 1, E-28040 Madrid, Spain*
[11]*Instituto de Física de Partículas y del Cosmos, IPARCOS, Fac. CC. Físicas, Universidad Complutense de Madrid, Plaza de las Ciencias 1, E-28040 Madrid, Spain*
[12]*Instituto de Astrofísica de Andalucía, IAA-CSIC, Glorieta de la Astronomía s/n, E-18008 Granada, Spain*
[13]*FRACTAL S.L.N.E. Calle Tulipán 2, portal 13, 1A, E-28231 Las Rozas de Madrid, Spain*

ABSTRACT

We present a spatially resolved spectroscopic study for the metal poor H II galaxy J084220+115000 using MEGARA Integral Field Unit observations at the Gran Telescopio Canarias. We estimated the gas metallicity using the direct method for oxygen, nitrogen, and helium and found a mean value of $12 + \log{(O/H)} = 8.03 \pm 0.06$, and integrated electron density and temperature of $\sim 161\,\mathrm{cm^{-3}}$ and $\sim 15400\,\mathrm{K}$, respectively. The metallicity distribution shows a large range of $\Delta(O/H) = 0.72$ dex between the minimum and maximum (7.69 ± 0.06 and 8.42 ± 0.05) values, unusual in a dwarf star-forming galaxy. We derived an integrated $\log{(N/O)}$ ratio of -1.51 ± 0.05 and found that both N/O and O/H correspond to a primary production of metals. Spatially resolved maps indicate that the gas appears to be photoionized by massive stars according to the diagnostic line ratios. Between the possible mechanisms to explain the starburst activity and the large variation of oxygen abundance in this galaxy, our data support a possible scenario where we are witnessing an ongoing interaction triggering multiple star-forming regions localized in two dominant clumps.

Key words: H II regions – galaxies: dwarf – galaxies: individual: J084220+115000 – ISM-galaxies: starburst.

1 INTRODUCTION

Observationally, H II Galaxies (HIIG)[1] and Giant H II Regions (GHIIRs) represent the youngest super star clusters (SSCs) that can be observed in any detail. In particular, the study of HIIGs

provides important clues about the intrinsic properties of young or unevolved galaxies. These clues are important in searches for primaeval galaxies, particularly if starbursts are the dominant mode of galaxy formation. Though their optical-UV light is clearly dominated by young stars, HIIGs are unlikely to be truly 'young' in the sense of completely lacking old stars (e.g Telles & Terlevich 1997). This was found even in the most extreme low abundance objects like IZw18 (e.g Aloisi et al. 2007; Annibali et al. 2013).

HIIGs have a high specific star-formation rate [$\log{(sSFR)} \sim -7$ to $-6.5\,\mathrm{yr^{-1}}$, Searle & Sargent 1972; Telles & Melnick 2018]. Studies indicate that the recent star formation is concentrated in extreme SSCs with sizes of $\sim 20\,\mathrm{pc}$ (e.g. Telles 2003) and low heavy-element abundance ($1/50 < Z < 1/3\,Z_\odot$). In fact, the most metal-poor compact starbursts at all redshifts tend to appear as HIIGs (Kunth & Östlin 2000; Gil de Paz, Madore & Pevunova 2003; Amorín et al. 2012;

[1] 'Peculiar' objects from Zwicky list of compact galaxies were identified by Sargent (1970a, 1970b) and further studied by Sargent & Searle (1970) (SS1970). Those that have spectral characteristics indistinguishable from giant extragalactic H II regions (like 30 Dor in the LMC) were designated by SS1970 as 'Isolated Extragalactic H II Regions'. Later on, these compact dwarf star forming galaxies were dubbed H II Galaxies (Campbell, Terlevich & Melnick 1986; Terlevich et al. 1991; Maza et al. 1991).

Izotov, Thuan & Guseva 2012; Kehrig et al. 2016; Amorín et al. 2017; Kehrig et al. 2018; Wofford et al. 2021).

Most HIIGs were discovered in objective-prism surveys thanks to their strong narrow emission lines. Currently, in spectroscopic surveys like the Sloan Digital Sky Survey (SDSS), they are selected by very large equivalent widths in the Balmer lines. Since the luminosity of HIIGs is dominated by the starburst component, they can be observed even at large redshifts, becoming interesting standard candles. (cf. Melnick, Terlevich & Terlevich 2000; Plionis et al. 2011; Terlevich et al. 2015; Chávez et al. 2016; Yennapureddy & Melia 2017; Ruan et al. 2019; González-Morán et al. 2019; Wu et al. 2020; González-Morán et al. 2021; Tsiapi et al. 2021).

Many of the properties of HIIGs are usually obtained from single aperture or long slit observations. The data are then used to derive the physical conditions of the gas (temperatures and densities) and to estimate abundances and ionization conditions, as well as characteristics of the ionizing star clusters (e.g. mass, age, effective temperature). These results constitute the main body of our knowledge of the conditions of the gas in HIIGs and GHIIRs (e.g. Pérez-Montero & Díaz 2005; Hägele et al. 2007; Pérez-Montero 2014).

The assumption is that the measurements derived from single aperture or long-slit are representative of the whole nebular conditions, and variations within the nebula are assumed to be minimal or non-existent. This scenario can also be supported by the fact that in general these types of studies do not find a significant abundance gradient or large deviation in kinematics properties in the ionized gas of HIIGs or GHIIRs, even for HIIGs showing multiple star-forming knots (Esteban & Peimbert 1995; Vilchez & Esteban 1996; Vílchez & Iglesias-Páramo 2003; Papaderos et al. 2006; Pérez-Montero & Contini 2009; Pérez-Montero et al. 2011; Esteban et al. 2020).

Integrated observations, such as long-slit or single fibre, may fail to correlate the spatial location of star-forming regions with the physical conditions and the chemical abundances of the interstellar medium (ISM) as derived from the optical emission lines. Traditionally, the physical conditions (age and metallicity of the ionizing clusters and the kinematics, and metallicity of the ionized gas) of metal-poor HIIGs have been derived from long-slit observations, either centred on the brightest regions or by several observations scanning the whole galaxy. Presently, integral field spectroscopy constitutes a powerful tool to obtain simultaneously information, not only on the brightest condensations but also on the diffuse matter surrounding them. This helps to understand better the interplay between the massive stars population and the properties of the Interstellar Medium in metal-poor galaxies as has been amply illustrated in the literature in recent years (e.g Lagos et al. 2009; Pérez-Montero et al. 2013; Kehrig et al. 2016, 2018; Bosch et al. 2019; Kumari et al. 2019; James et al. 2020; Bresolin et al. 2020; Wofford et al. 2021; Carrasco et al. 2022).

Our main motivation in this paper is to present a study of the spatiall resolved properties of the ionized gas of the metal-poor HIIG: SDSS J084220.94+115000.2 (hereafter, J0842+1150) that shows multiple bursts of star formation that can be identified in the *Hubble Space Telescope* (*HST*) image and in the *Chandra* data. This study is based in observations obtained at the Gran Telescopio Canarias (GTC), using the integral field unit (IFU) of the instrument MEGARA (acronym of Multi-Espectrógrafo en GTC de Alta Resolución para Astronomía). GTC is located at the Observatorio del Roque de los Muchachos in la Palma, Canary Island, Spain.

The paper is organized as follows: In Section 2, we present a complete description of the H II galaxy J0842+1150. In Section 3, we describe the observations and data reduction. In Section 4, we report

the flux measurements and optical emission line intensity maps. In Section 5, we derived from the observations the maps of the properties of the ionized gas. Abundance maps for helium, oxygen, and nitrogen derived from the direct method based on determinations of the electron temperature are presented in Section 6. In Section 7, we compare strong-line methods to derive abundances for the individual spaxels and discuss the nitrogen to oxygen abundance ratio for J0875+1150. In Section 8, we discuss the chemical inhomogeneities in HIIGs and Blue Compact Dwarf galaxy (BCD) for the case of J0842+1150. Finally, in Section 9, we present a summary of this work and our main conclusions.

2 THE H II GALAXY J0842+1150

J0842+1150 also known as Cam 0840+1201 was reported for the first time by Campbell et al. (1986), as a low-metallicity HIIG with values of O/H = 0.785×10^{-4} ($12 + \log{(O/H)} = 7.89$) and N/H = 0.270×10^{-5} ($12 + \log{(N/H)} = 6.43$) with an electron temperature of $T_e[O\,III] = 13891$ K. Using *International Ultraviolet Explorer* (*IUE*) observations, Terlevich et al. (1993) detected Ly α emission in this galaxy.

In the morphological classification scheme for HIIGs by Telles, Melnick & Terlevich (1997), J0842+1150 was reported as an HIIG with perturbed and extended morphology, with two dominant giant H II regions and signs of tails beyond the star-forming regions. They reported an oxygen abundance of $12 + \log{(O/H)} = 7.88$ and a velocity dispersion of 36.5 km s^{-1}. J0842+1150 appears to be an interacting galaxy consisting of two clumps of multiple star-forming regions, each one with unresolved X-ray emission, detected at 0.5–8 keV by Brorby & Kaaret (2017).

Kehrig, Telles & Cuisinier (2004), analysing the chemical abundances in HIIGs with a detailed spectroscopic study, report abundances of $12 + \log{(O/H)} = 7.82 \pm 0.08$ and $12 + \log{(S/H)} = 6.36 \pm 0.33$ with a $T_e[O\,III]$ of 13600 ± 600 K. Brinchmann, Kunth & Durret (2008) classified it as a Wolf–Rayet (WR) galaxy and also derived an abundance of $12 + \log{(O/H)} = 8.09$ using the direct T_e method and the SDSS spectrum. Bordalo & Telles (2011) found a metallicity ($12 + \log{(O/H)}$) of 7.98 and also reported a velocity dispersion in km s^{-1} of 36.8 ± 1.8, 34.9 ± 0.4, 34.6 ± 0.7, and 34.4 ± 0.2 for the H β, H α, and [O III] $\lambda\lambda4959,5007$ lines, respectively. Whereas Chávez et al. (2012) reported 32 ± 3 km s^{-1} for H β and 27 ± 1 km s^{-1} in [O III]. The different values reported in the literature may be due to a pointing problem.

2.1 Is J0084220 a Lyman break analogue?

Interestingly, J0084220 shows similar shapes to those that have been reported in local nearby compact UV-luminous galaxies (UVLGs) that closely resemble high-redshift Lyman break galaxies (LBGs), sometimes called 'Lyman break analogues' (LBAs). Analysis of their SDSS spectra and of their spectral energy distributions has shown that the LBAs are similar to LBGs in their basic global properties, thus enabling a detailed investigation of many processes that are important in star-forming galaxies at high redshift. Common characteristics include faint tidal features and UV/optical light dominated by unresolved ($\sim$100–300 pc) super-starburst regions (SSBs), suggesting that the starbursts are the result of a merger or interaction (Grimes et al. 2007; Overzier et al. 2008, 2009; Basu-Zych et al. 2009; Gonçalves et al. 2010).

Additional properties for LBA are stellar masses as low as $10^{8.5}$ M$_\odot$ and $12 + \log{(O/H)} < 8.5$ with particular detection of X-ray emission (Brorby et al. 2016) which match the properties of the most luminous

Table 1. J0842+1150 general properties.

Parameter	Value
RA (J2000)	$08^h42^m20^s.90$
Dec. (J2000)	$+11°50'00''.2$
Redshift	0.029^a
D_L(Mpc)	125.2^b
Metallicity (12 + log (O/H))	$8.09 ± 0.01^c$
SFR ($M_\odot$ yr^{-1})	7.2^d
$L_X(10^{39}$ erg s^{-1})	$36 ± 7.5^e$
SDSS u	17.07^f
SDSS r	16.63^f
log L(Hβ)(erg s^{-1})	$40.85 ± 0.13^f$
R$_{50}$ (r band)	2.81 arcmin ∼
	1.65 kpc ^{f}

^{a}Spectroscopic redshift as reported by SDSS ^{b}Luminosity distance in Mpc (from SDSS redshift). The Hubble Constant adopted throughout this work is H_0= 71.0 km s^{-1} Mpc^{-1}, assuming a flat Universe and a ΛCDM cosmological model with $\Omega_m = 0.3$. ^{c}Oxygen abundance derived using the T_e-method and the Sloan fibre (Brinchmann et al. 2008) ^{d}Star-formation rate (SFR) from UV + IR ^{e}Total X-ray luminosity (L$_X$) refers to the 0.5–8 keV band flux assuming a photon index of $\Gamma = 1.7$ reported by Brorby & Kaaret (2017) ^{f}Parameters as reported or derived from SDSS.

HIIGs. Using the FUV flux from Rosa-González, Terlevich & Terlevich (2002), we derived a $L_{FUV} = 10^{10.13} L_\odot$ and adopting the radius in the u-band from the SDSS reported in Chávez et al. (2014), we derived a I_{FUV} of $10^{9.07} L_\odot$ kpc^{-2}. Combined with the morphology, this places J084220+11500 as a potential candidate for LBA which motivates the study of this galaxy and also a larger sample of HIIGs in the context of LBAs and Lyman α Emitters and the precise connection between them. Thus, J084220+11500 provides a local laboratory to study the extreme star formation processes that could be occurring in high-redshift galaxies.

In Table 1, we list the main properties of J0842+1150. It has to be indicated that the spectroscopic parameters were derived from single aperture data that do not cover the total nebular emission. In Fig. 1, we present the *HST* image of J0842+1150 in the F336W filter, the field of view (FoV) of MEGARA IFU in blue, the SDSS fibre as a cyan–dashed circle, the X-ray emission contours (0.5–8 keV) from Brorby & Kaaret (2017) in green, and in white the contours of the flux of the Hα map derived in this work as described in Section 4. Throughout this work, we also present our MEGARA results obtained for integrated regions R1 and R2 corresponding to main star-forming bursts identified by means of the Hα contours; we also present integrated regions according to the metallicity variation [see the details in Appendix A (Supplementary Material)].

3 OBSERVATIONS AND DATA REDUCTION

3.1 Observations

Spectroscopic observations of J0842+1150 were carried out using the IFU of MEGARA at the 10.4 m GTC. MEGARA provides integral-field and multi-object spectrograph at low, medium, and high spectral resolution R_{FWHM}^2 ∼6000, 12 000, and 20 000, respectively for the LR, MR, and HR modes in the visible wavelength interval covering from 3650 to 9700 Å, through 18 spectral configurations: 6 in LR, 10 in MR, and 2 in HR.

$^2R_{FWHM} \equiv \lambda/\Delta\lambda$ with $\Delta\lambda$ = individual lines full width at half maximum (FWHM).
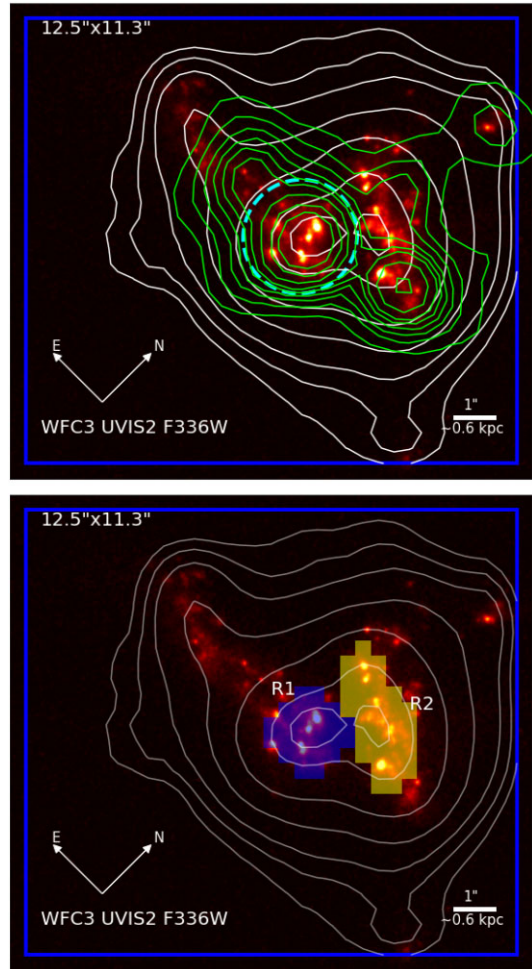

Figure 1. *HST* WFPC3/F336W archival image of J0842+1150 (*HST*, Proposal ID 13940; PI: Matt Brorby). The blue box denotes MEGARA IFU field of view (12.5×11.3 arcsec^2). In the top panel, the cyan–dashed circle shows the position of the SDSS 3 arcsec fibre diameter. The 0.5–8 keV X-ray contours (from Brorby & Kaaret 2017) are shown in green. Bottom panel: masked regions where spectra were extracted to analyse individual regions (R1,R2). Here and in all subsequent figures, white contours correspond to the Hα emission map obtained in this work.

In particular, we used the integral field unit mode. MEGARA IFU data consist of 623 spectra, of which 567 are on object which provide a FoV of 12.5×11.3 arcsec^2. 56 fibres are reserved for the sky (eight mini bundles of seven fibres each) located at the edge of the field at distances from 1.7 to 2.5 arcmin from the centre of the IFU designed to perform simultaneous sky subtraction. The observations were carried out with a rotated FoV of 45° in order to minimize the contamination of background galaxies on the sky bundles.

The data were obtained using three different gratings in order to cover the main optical emission lines. LR-U, LR-B, and LR-R; the covered wavelength and resolving power of each grating are presented in Table 2. The FoV of MEGARA corresponds to 7.2×6.5 kpc at the distance of the galaxy (125.2 Mpc, see Table 1 and Fig. 1), with spatial sampling of 0.62 arcsec per spaxel.^{3}

^{3}This size corresponds to the diameter of the circle on which the hexagonal spaxel is inscribed (∼355 pc).

Table 2. Observation set-up, 2020 November 23rd.

Grating	Wavelength range (Å)	Central wavelength (Å)	R_{FWHM}	Exp. time (s)	Airmass
VPH405-LR (LR-U)	3654–4391	4025	5750	900×3	1.05
VPH480-LR (LR-B)	4332–5199	4785	5000	600×3	1.08
VPH675-LR (LR-R)	6096–7303	6729	5900	600×3	1.09

A total of 1.75 h on the galaxy in dark sky and spectrophotometric conditions were observed, with the integration times split in three exposures for each gratings as indicated in Table 2. The seeing was about 1 arcsec during the observations in each spectral configuration, corresponding to different volume phase holographic gratings (VPH) and all science frames were obtained at similar airmasses close to unity. Additionally, all necessary calibration frames were acquired i.e. spectrophotometric standard stars, halogen lamp flats, ThNe arcs, and a series of bias frames.

3.2 Data reduction

The data reduction procedure was carried out using MEGARA Data Reduction Pipeline (DRP)[4] publicly available and open source under GPLv3+ (GNU Public License, version 3 or later). The DRP is a custom-made user-friendly tool formed by a set of processing recipes developed in PYTHON (Pascual et al. 2019) which is based on a series of processing recipes and the cookbook.[5] The recipes used for obtaining the calibration images were MegaraBiasImage, MegaraTraceMap, MegaraModelMap, MegaraArcCalibration, MegaraFiberFlatImage, MegaraLcbStdStar.

Briefly, the data reduction starts generating a Master Bias with the MegaraBiasImage routine from the bias images. Images are corrected from overscan and trimmed to the physical size of the detector. To trace the locus of each of the 623 spectra, the MegaraTraceMap recipe uses the halogen lamp images to find the position of the illuminated fibres on the detector. The MegaraModelMap recipe takes the results of the previous step and the halogen images as input to produce an optimized extraction of the fibre spectra. The routine fits simultaneously 623 Gaussians every 200 columns and then interpolates the parameters of the Gaussian for each spectral pixel. With this information, the routine generates a weight map for every fibre which is applied to the data in order to perform the extraction.

The MegaraArcCalibration recipe uses the lamp wavelength calibration images, their offset value and the output of the MegaraModelMap to produce a wavelength calibration. The MegaraFiberFlatImage recipe is used to correct for the global variations in transmission between fibres and as a function of wavelength. The MegaraLcbAcquisition recipe returns the position of the standard star on the IFU. Once the position of the standard star on the LCB is known, the MegaraLcbStdStar routine produces the Master Sensitivity curve by comparing the 1D flux spectrum of the standard star (corrected from atmospheric extinction) with its tabulated flux-calibrated template. This sensitivity curve also corrects from the spectral instrument response (mostly dominated by VPH transmission and detector quantum efficiency), so that this step is needed even when non-photometric conditions prevent a reliable flux calibration.

Once all the calibration files are obtained, the science frames are processed with the recipe MegaraLcbImage producing the Row-Stacked-Spectra (RSS) file with the individual spectra for all fibres, wavelength, and flux calibrated and corrected for telluric effects.

Finally, we created data cubes with a spaxel scale of 0.4 arcsec in each of the spatial axes, from the RSS file using create_cube_from_rss.[6]

4 FLUX MEASUREMENTS AND EMISSION LINE INTENSITY MAPS

In what follows, we describe the analysis performed to obtain the emission line fluxes. Each observing set-up is characterized by different coverage, central wavelength, and spectral resolution as described in Table 2. We used LR-U to measure the doublet [O II] $\lambda\lambda$3727, 29 Å and Hδ, LR-B for Hγ, [O III] λ4363, Hβ, [O III] $\lambda\lambda$4959, 5007, and LR-R for [O I] λ6302, Hα, [N II] λ6583, and [S II] $\lambda\lambda$6716, 6730 Å.

Emission line fluxes were measured from individual spaxels by fitting single Gaussian curves to the profiles using a least-squares minimization procedure implemented in the PYTHON package LMFIT (Newville et al. 2014). For each spaxel, we first averaged the spectrum by considering a box/squared region with a size comparable to the point spread function (PSF) of the observation (2 spaxels). This improves the S/N of the emission line. We fitted a straight line to remove a local continuum using two spectral windows at both sides of the emission lines; those emission line free regions were used also to measure the RMS. The fluxes for the integrated regions and the SDSS spectrum are presented in Table 3.

To consider the uncertainties associated with the emission line fluxes, we generated a synthetic emission line adding randomly the noise of the continuum (RMS) to the observed spectra and repeated the fit; for each spaxel, 200 iterations were performed to estimate the final errors. Finally, we exclude spaxels that have lines with peak signal-to-noise (S/N, with S the amplitude of the line and N the RMS in the continuum) lower than 4.

The individual spectra for regions R1 and R2 are shown in Fig. 2, where we also included the integrated spectrum created by adding the flux in all the spaxels with S/N(Hα) (per spaxel) $\geq$4 enclosing basically all the nebular emission across the FoV. In Fig 3, we show individual profiles of the most intense emission lines normally found in HIIGs. In table

The intensity maps, derived from the Gaussian fits, are presented in Fig. 4, the errors associated to the emission-line fluxes estimated by means of the bootstrap method are between 7 per cent for the

---

[4] https://github.com/guaix-ucm/megaradrp
[5] http://doi.org/10.5281/zenodo.3834345

[6] create_cube_from_rss, available in the megaradr repository, is a tool written in PYTHON to convert MEGARA reduced data products from the RSS format obtained with megaradrp to a more user-friendly 3D data cube.

Table 3. Emission line fluxes and physical properties from selected regions and SDSS fibre.

Wavelenght (Å)	Region 1 (R1)	Region 2 (R2)	Integrated	SDSS fibre
3727 [O II]	147.6 ± 5.0	190.3 ± 5.1	905.3 ± 54.2	162.0 ± 2.6
3729 [O II]	203.8 ± 4.9	274.2 ± 5.1	1345.3 ± 56.1	143.7 ± 2.4
3869 [Ne III]	72.7 ± 1.6	123.3 ± 2.5	464.6 ± 18.4	72.4 ± 1.0
3889 H I + He I	39.0 ± 1.7	66.7 ± 1.9	258.2 ± 19.5	37.1 ± 0.9
3968 [Ne III]	18.5 ± 1.5	38.2 ± 1.9	136.1 ± 17.9	50.1 ± 1.2*
3970 H ϵ	30.4 ± 1.5	50.5 ± 1.9	189.2 ± 16.0	50.1 ± 1.2*
4102 H δ	51.0 ± 1.2	82.9 ± 1.7	306.3 ± 13.3	48.5 ± 1.5
4341 H γ	61.4 ± 0.7	86.9 ± 1.8	321.4 ± 3.0	81.2 ± 1.0
4363 [O III]	7.4 ± 0.3	15.7 ± 0.5	47.1 ± 2.9	9.1 ± 0.4
4471 He I	5.4 ± 0.2	7.6 ± 0.3	29.5 ± 2.9	8.1 ± 0.5
4658 [Fe III]	1.7 ± 0.2	1.8 ± 0.3	7.1 ± 2.1	3.4 ± 0.2
4686 He II	0.8 ± 0.2	1.6 ± 0.3	3.4 ± 1.7	–
4711 [Ar IV]	1.0 ± 0.3	1.5 ± 0.3	5.6 ± 2.9	–
4713 He I	–	1.0 ± 0.3	5.6 ± 2.9	–
4740 [Ar IV]	0.7 ± 0.2	1.0 ± 0.2	7.9 ± 4.6	–
4861 H β	151.2 ± 0.7	209.7 ± 1.2	744.2 ± 6.7	185.4 ± 1.5
4922 He I	1.6 ± 0.2	1.8 ± 0.3	9.9 ± 3.4	0.8 ± 0.2
4959 [O III]	239.0 ± 1.1	343.7 ± 2.3	1114.3 ± 12.1	294.2 ± 2.3
4988 [Fe III]	2.6 ± 0.2	3.0 ± 0.21	12.2 ± 2.0	1.2 ± 0.3
5007 [O III]	712.7 ± 4.2	1027.0 ± 7.6	3333.9 ± 34.9	885.2 ± 6.0
5016 He I	2.5 ± 0.3	3.5 ± 0.2	14.6 ± 2.8	–
6302 [O I]	4.9 ± 0.2	5.9 ± 0.2	25.6 ± 1.8	8.4 ± 2.3
6312 [S III]	2.3 ± 0.2	2.8 ± 0.2	6.7 ± 1.4	5.4 ± 0.6
6364 [O I]	2.0 ± 0.2	2.3 ± 0.2	11.7 ± 1.9	3.1 ± 0.4
6547 [N II]	5.4 ± 1.3	4.7 ± 1.9	21.9 ± 9.0	–
6563 Hα	422.4 ± 1.3	544.1 ± 1.9	2045.5 ± 8.4	686.6 ± 5.2
6583 [N II]	14.6 ± 1.3	12.5 ± 1.9	63.1 ± 8.1	26.2 ± 0.3
6678 He I	3.6 ± 0.2	4.2 ± 0.2	17.9 ± 2.0	–
6716 [S II]	25.6 ± 0.2	26.9 ± 0.3	133.4 ± 2.4	47.0 ± 0.6
6730 [S II]	19.8 ± 0.2	20.4 ± 0.3	103.1 ± 2.3	32.9 ± 0.5
7065 He I	3.6 ± 0.7	4.7 ± 0.8	18.4 ± 8.1	8.7 ± 0.6
A_v	0.601 ± 0.15	0.452 ± 0.12	0.521 ± 0.11	0.673 ± 0.16
$Q \times 100$	0.02	0.0	0.0	0.01
L(Hβ)(erg s^{-1})	40.73 ± 0.14	40.78 ± 0.11	41.23 ± 0.12	40.85 ± 0.13
EW(Hβ)	172 ± 6	214 ± 8	102 ± 4	117 ± 5
EW(Hα)	458 ± 11	592 ± 9	238 ± 5	656 ± 11
n_e([S II]) (cm^{-3})	153 ± 59	159 ± 85	161 ± 54	152 ± 38
T_e([O III])$\times 10^4$ (K)	1.25 ± 0.05	1.41 ± 0.06	1.54 ± 0.08	1.23 ± 0.04
$12 + \log$ (O$^+$/H$^+$)	7.71 ± 0.06	7.49 ± 0.07	7.61 ± 0.07	7.66 ± 0.06
$12 + \log$ (O^{++}/H$^+$)	7.91 ± 0.05	7.77 ± 0.06	7.82 ± 0.06	7.94 ± 0.05
$12 + \log$ (O/H)	8.13 ± 0.06	7.91 ± 0.06	8.03 ± 0.06	8.12 ± 0.05
$\log$ (N/O)	− 1.41 ± 0.05	− 1.57 ± 0.05	− 1.51 ± 0.05	− 1.47 ± 0.05
$12 + \log$ (He$^+$/H$^+$)	10.81 ± 0.03	10.79 ± 0.03	10.84 ± 0.03	10.84 ± 0.03
Velocity dispersion measurements (km s^{-1})				
σ(Hβ)	35.3 ± 1.5	33.9 ± 1.5	37.9 ± 1.4	
σ([O III] λ4959)	33.2 ± 1.2	30.2 ± 1.3	34.9 ± 1.1	
σ([O III] λ5007)	33.4 ± 1.4	30.5 ± 1.3	35.1 ± 1.3	
σ(Hα)	35.7 ± 1.1	34.3 ± 1.1	38.0 ± 1.3	

Note. Fluxes are in units of 10^{-16} erg cm^{-2}s^{-1}. * In the SDSS spectrum, the emission lines [Ne III] λ3969 and H ϵ (λ3970) are blended. Here, we report the sum of the two lines for the SDSS. The velocity dispersion was obtained from the FWHM of the Gaussian fit to the profile of the emission lines and corrected by thermal, instrumental, and fine structure (σ_{fs} for H β and H α lines only) broadening.

fainter lines (e.g. [O III] λ4363, [N II] λ6583 [S II] $\lambda\lambda$6716,30) and 2 per cent for the strong lines (e.g H α, H β, [O III] λ5007).

5 SPATIALLY RESOLVED PROPERTIES OF THE IONIZED GAS

5.1 Extinction correction

Massive bursts of star formation are embedded in large amounts of gas and dust. The latter is responsible for a wavelength-dependent light extinction along the line of sight due to absorption and scattering. Usually the amount of extinction is estimated using hydrogen recombination lines through the Balmer decrement, although con-

tamination by underlying stellar Balmer absorption lines (especially for high-order ones) changes the ratio of the observed emission lines such that the internal extinction could be overestimated.

To correct for extinction, we used a modification of the Balmer decrement method. We corrected the Balmer line emissions for the effect of stellar absorption lines using the technique proposed by Rosa-González et al. (2002). This method allows us to obtain simultaneously the values of the visual extinction, A_V, and the underlying stellar absorption, Q. In Fig. 5, we show the Balmer decrement plane $\log(F(H\alpha)/F(H\beta))$ versus $\log(F(H\gamma)/F(H\beta))$. Extinction and underlying absorption vectors are indicated by the yellow and black arrows, respectively in Fig. 5. In the absence of underlying absorption, all points should be distributed along the
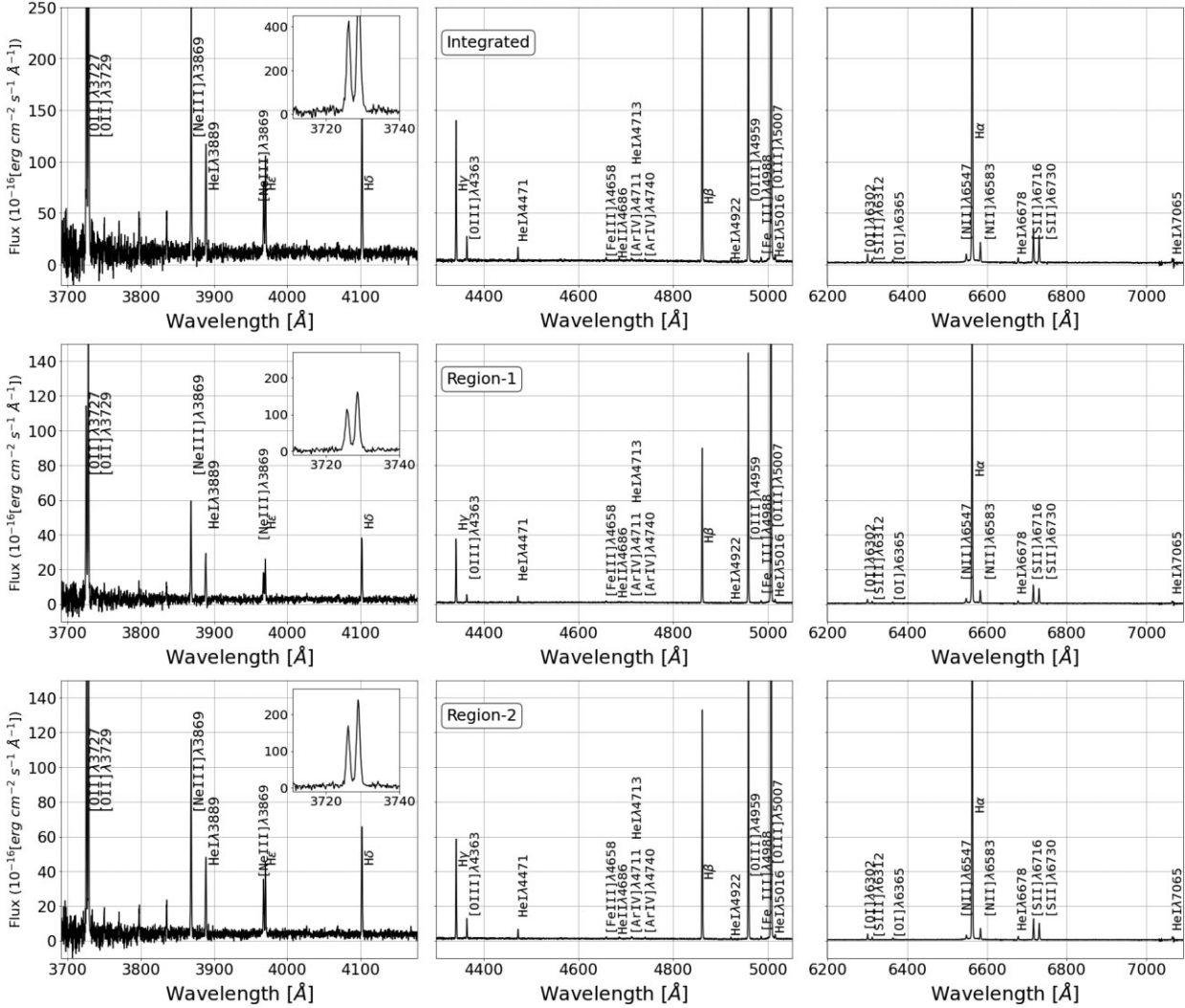
Figure 2. Flux-calibrated spectra for J0842+1150 integrated regions. From left to right, VPH405-LR, VPH480-LR, VPH675-LR. The inset in the left column shows a zoom to the region of the [O II] doublet. The label in the middle panel indicates the region where the spectrum has been obtained from.

extinction vector, while in the absence of extinction all points should be distributed along the underlying absorption line.

We calculated A_V and Q using the theoretical ratios for case B recombination $F(H\alpha)/F(H\beta) = 2.86$ and $F(H\gamma)/F(H\beta) = 0.47$ (Osterbrock [1989](#)). These ratios are weakly sensitive to density but have larger variations due to temperature. In Fig. [5](#), we plot two gray bands corresponding to these variations due to temperatures between 5000 and 20 000 K reported by Groves et al. ([2012](#)); within the errors, our spaxels fall within these regions. We measured the Balmer lines from the flux maps and propagated the uncertainties by a Monte Carlo procedure. Errors in the luminosities are dominated by uncertainties in the extinction correction. In cases where the flux ratio is lower than the theoretical value, we assume a 0 value for the extinction. The dereddened fluxes for each spaxel are obtained from the expression:

$$F_0(\lambda) = F_{obs}(\lambda)10^{0.4A_V k(\lambda)/R_V} \tag{1}$$

where $k(\lambda) = A(\lambda)/E(B-V)$ is given by the extinction law from Gordon et al. ([2003](#)), and $R_V = A_V/E(B-V)$ is the optical total-to-selective extinction. We adopted $R_V = 2.77$ corresponding to the LMC2 supershell near the 30 Doradus star-forming region,

the prototypical GHIIR in the Large Magellanic Cloud. This value is the result of the LMC2 supershell sample average. Finally, the dereddened fluxes are corrected by the underlying absorption:

$$F(\lambda) = \frac{F_0(\lambda)}{1-Q} \tag{2}$$

Fig. [6](#) shows the maps of equivalent width for $H\beta$ and $H\alpha$ and the intensity ratios $H\alpha/H\beta$ and $H\gamma/H\beta$ normalized to their theoretical values and the maps corresponding to A_V and Q. Although this last correction is necessary, in this case, it does not affect the results. The stellar continuum is very low and stellar absorptions are not detected in the spectra.

5.2 Diagnostic diagrams maps

By combining the flux maps of different emission lines, we created the spatially resolved BPT diagrams (Baldwin, Phillips & Terlevich [1981](#)), widely used to differentiate the excitation mechanism for star-forming galaxies from AGN. The spatial distribution for the BPT line ratios of [O III] $\lambda5007/H\beta$, [O I] $\lambda6300/H\alpha$, [N II] $\lambda6584/H\alpha$, and [S II] $\lambda\lambda6717,31/H\alpha$ are displayed in Fig. [7](#). The line ratios are not
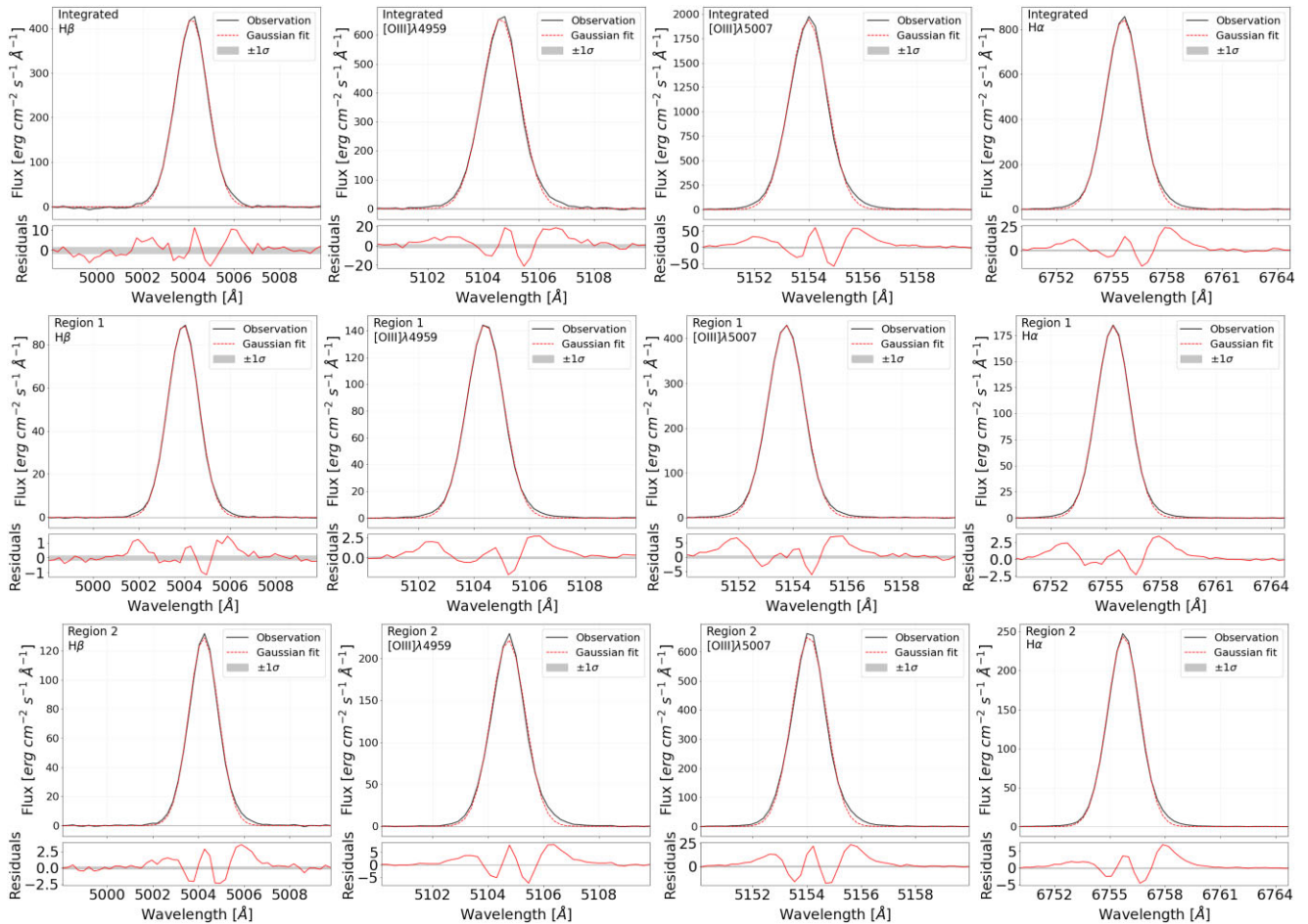
Figure 3. Line profiles (H β, [O III] λ4959, [O III] λ5007 and H α) and Gaussian fits for the individual regions and the integrated spectrum on the nebular emission.

corrected for extinction, but this is expected to be a minor effect as the ratios involve lines which are close to each other in wavelength.

Spatially resolved BPT diagrams for J0842+1150 are shown in Fig. 8: [O III] λ5007/H β versus [N II] λ6584/H α, [S II] λ6717, 31/H α, and [O I] λ6300/H α. Each point corresponds to one spaxel, with line detection threshold of $\geq$4 for each line. Fig. 8 shows that for every position in the galaxy our emission-line ratios fall in the star-forming region according to the empirical classification line of Kauffmann et al. (2003) and theoretical upper bound to pure star formation given by Kewley et al. (2006), i.e. below and to the left of the separation lines in all BPT diagrams, specifically, in the high-excitation and low-metallicity region. This suggests that photoionization from hot massive stars appears to be the dominant excitation mechanism within the nebular region of J0842+1150.

For comparison purposes, we separated into two regions the star-forming galaxies according to the equivalent width in the H β line corresponding to the main criteria to choose samples of HIIGs. In Fig. 8, we also plot local SDSS star-forming galaxies (DR16) separated by the EW(H β). The green contours correspond to EW(H β) $\geq$ 50 Å and black contours to EW(H β) < 50 Å. This value of EW(H β) corresponds to an upper limit in the age of 5 Myr assuming an instantaneous starburst model, i.e. that all stars are formed simultaneously in a short-living starburst episode. For individual spaxels and integrated regions, the results are consistent with the location of the HIIGs as can be seen in the lower panels,

which are a zoom to the region of high ionization and low metallicity consistent with EW(H β) $\geq$ 50 Å.

The spectra of individual spaxels occupy a narrow band on the BPT diagram consistent with the region characterized by star formation. The offset seen in the BPT diagrams of individual spaxels with respect to the SDSS H II galaxies is apparent and corresponds to the density of points that we plot for H II galaxies which have a median value of 43 Å in the EW(H β). Higher values of EW(H β) tend to populate a higher region in this diagram showing a sequence in EW(H β) (e.g. Curti et al. 2022) (or equivalently, specific star formation rate). In our case, the EW(H β) values for J0842+1150 are even greater than 50 Å in many spaxels. In the case of [O I] λ6300/H α, we do not have enough spaxel [O I] λ6300 detections towards low EW(H β) values.

5.3 Electron density

The quality of the spectra with the detection of weak emission lines, allows us to determine the T_e and n_e and hence the metallicity using the direct method as well as other physical conditions of the gas.

We have used the PYTHON package PYNEB[7] (Luridiana, Morisset & Shaw 2015) to compute the physical properties and ionic oxygen

---

[7]An innovative code for analysing emission lines. PYNEB computes physical conditions and ionic and elemental abundances and produces both theoretical
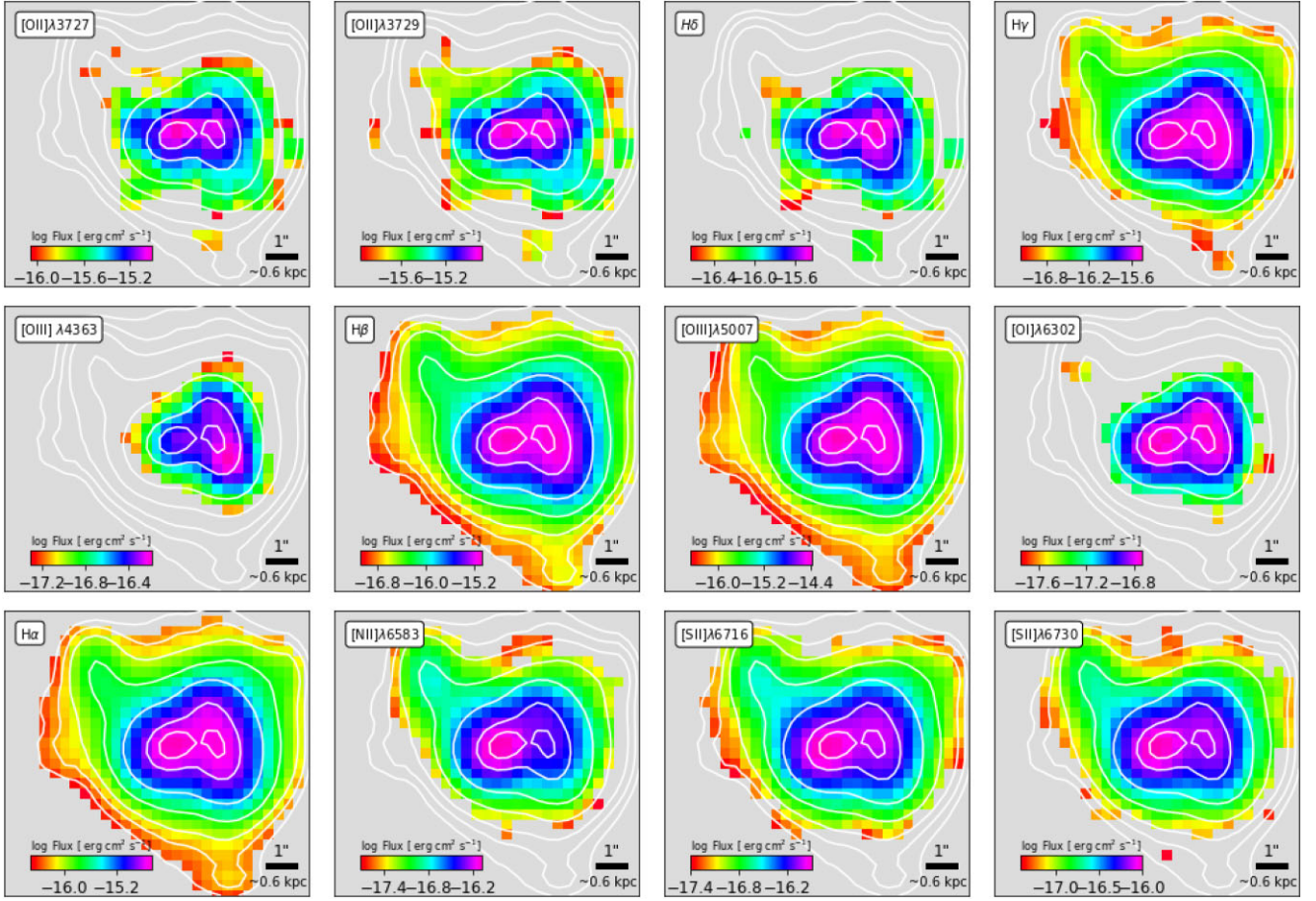
Figure 4. Emission line flux maps of J0842+1150: [O II] λ3727, [O II] λ3729, H δ, H γ, [O III] λ4363, H β, [O III] λ5007, [O I] λ6302, H α, [N II] λ6583, [S II] λ6716, and [S II] λ6730. Only fluxes with S/N ≥ 4 are shown. The spaxels with no measurements available or below the S/N cut are left grey. Isocontours of the H α flux are shown for reference as in Fig. 1.
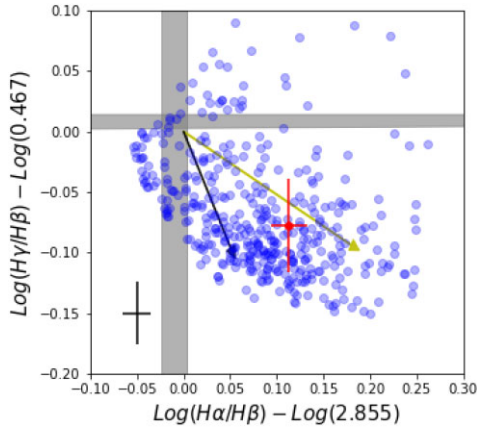

Figure 5. Balmer decrements for the spaxels with S/N ≥ 4 in the Balmer lines normalized to the theoretical values. The red circle marks the value derived from the SDSS spectrum. The black cross at the bottom left represents the mean error of the blue points. The vector due to pure extinction is shown in yellow; the black one shows the effect of an underlying stellar population. The vertical and horizontal bands correspond to the Balmer decrement theoretical values reported by Groves, Brinchmann & Walcher (2012).

abundances in a homogeneous way using the relevant line intensity ratios.

The electron density, n_e and electron temperature were calculated simultaneously from the [S II] λ6717/[S II] λ6731 line ratio and [O III] λ4363/[O III] λ5007, respectively. We used the atomic data and collision strengths from Rynkun, Gaigalas & Jönsson (2019) and Tayal & Zatsarinny (2010), respectively given by the default dictionary in PYNEB. The errors have been obtained using a bootstrap method. For each spaxel, we propagated the error in the lines intensity, in the extinction correction, computed the line intensity ratios, and ran pyneb. This process is repeated 100 times per spaxel. We obtain a distribution of density for each spaxel and take the median as the value of the spaxel and the standard deviation as a measure of the associated error.

Fig. 9 shows the density maps, the associated error distribution maps and the histogram of density values across the galaxy derived from the [S II] λ6717/[S II] λ6731 line-intensity ratio. We found a homogeneous density distribution from 70 to 300 cm^{-3} with errors varying from 50 to 100 cm^{-3}, and an average value of 153 ± 59 cm^{-3}. The structure observed in the density maps is not significant at more than 1σ.

and observational diagnostic plots; we used the version 1.1.14 https://github.com/Morisset/PyNeb_devel/tree/master/docs
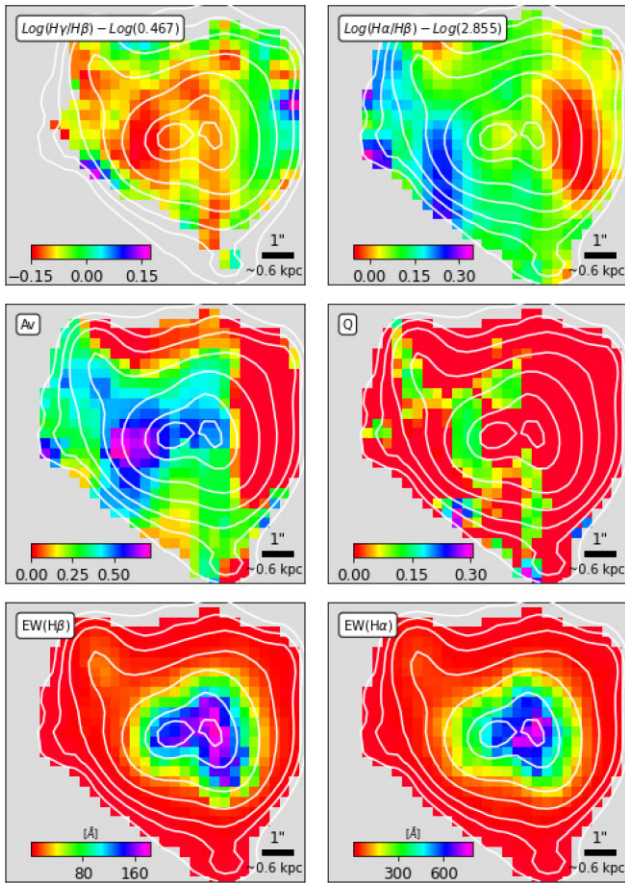
Figure 6. Upper panels: Balmer lines intensity ratio Hγ/Hβ (left) and Hα/Hβ (right). Middle panels: visual extinction (A_V) and underlying stellar absorption (Q). Bottom panels: distribution of the equivalent width of Hβ and Hα.

We also computed the electron density using the ratio of [O II] $\lambda3729/\lambda3726$ and the atomic data of [O II] from Zeippen (1982) and collision strengths from Kisielius et al. (2009). The electron density distribution of the nebular emission derived from the [O II] $\lambda3729/\lambda3726$ is lower than the values derived using the sulphur lines, with a maximum of $250\,\text{cm}^{-3}$ and minimum of $30\,\text{cm}^{-3}$ with errors between 50 and $160\,\text{cm}^{-3}$, and an average value of 112 ± 50. Within errors, the results are consistent and do not affect the analysis and subsequent results. Fig. 10 shows the density derived using the [O II] lines.

5.4 Electron temperature

The intensity ratios of selected forbidden lines are highly sensitive to T_e and thus are normally used to calculate it. For example the ratio of [O III] $\lambda4363/(\lambda5007 + \lambda4959)$ and [N II] $\lambda5755/(\lambda6459 + \lambda6583)$ among others (see e.g. Hägele et al. 2007, for a comprehensive description of the physical conditions in HIIGs), but the main disadvantage is that the auroral lines such as [O III] $\lambda4363$ or [N II] $\lambda5755$ are weak and therefore not detected if the observations are not deep enough or the metallicity of the region goes up.

The MEGARA VPHs used in this work and MEGARA resolution allow us to detect and to deblend the weak line of [O III] $\lambda4363$ across the main knots of nebular emission in the galaxy with enough S/N to obtain a reasonable estimate of the electron temperature using the ratio of [O III] $\lambda4363/\lambda5007$.
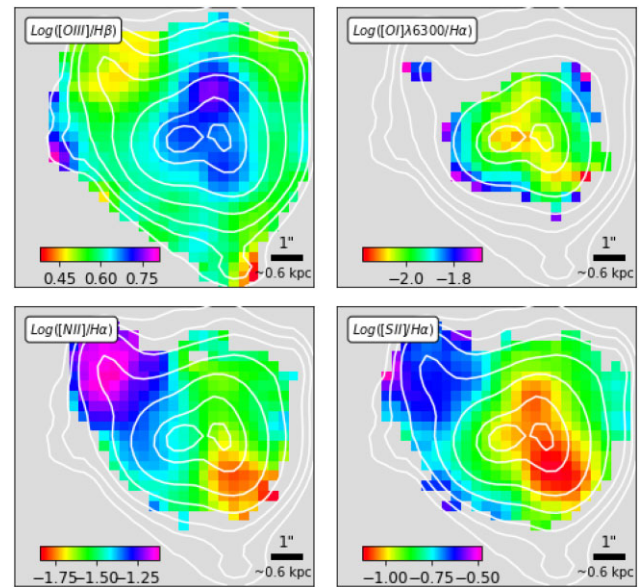
Figure 7. Maps of the diagnostic line ratios in logarithmic scale. The inset indicates the line ratios [O III] $\lambda5007$/Hβ, [O I] $\lambda6300$/Hα, [N II] $\lambda6584$/Hα and [S II] $\lambda\lambda6717,31$/Hα.

We used the intensity ratio of [S II] $\lambda6717/\lambda6731$ and [O III] $\lambda4363/\lambda5007$ to constrain the electron density and temperature at the same time, making use of the diagnostics class `getCrossTem-Den` in `PyNeb`, which allows simultaneous determination of the temperature and density by fitting two different line ratios. This command returns the density and temperature, which can be used in subsequent calculations as for the determination of ionic abundances. The errors are obtained in the same way as for the electron density.

Measuring the fluxes of very faint emission lines, e.g. [O III] $\lambda4363$, can lead to an overestimate of the intensity of the line (e.g. Rola & Pelat 1994; Kehrig et al. 2004, 2016). To check if our determination of electron temperature is affected by our measurement errors, we plotted the relation between T_e[O III] and the S/N of the [O III] $\lambda4363$ line in Fig. 11; no systematic effects are observed. This is evidence that the largest values of T_e[O III] that we derived here are not a consequence of putative flux overestimates on the [O III] $\lambda4363$ line.

Fig. 11 displays the distribution of the T_e([O III]) which shows values varying from nearly 11000 to 17000 K with errors between 400 and 1000 K. These values are normally found for individual HIIGs (e.g. Hägele et al. 2008; Pérez-Montero & Contini 2009) and more recently by Pérez-Montero et al. (2021) where they present the distribution of more than 1000 extreme emission-line galaxies in SDSS and find a mean value of 12100 K, with a standard deviation of 1800 K.

The maps of T_e with its error and the histogram of the T_e distribution are shown in Fig. 12. We also compute n_e[O II], from the ratio of [O II] $\lambda3729/\lambda3726$, to derive T_e[O III] and the results are shown in Fig. 13. We did not find significant variations in the electron temperature distribution using either density indicator.

The values found here are lower than values reported for IZw18, one of the most metal-poor galaxies in the local Universe, and for which the temperature ranges between 15000 and 22000 K (Kehrig et al. 2016), similar to the range found in SBS 0335−052E, a metal-poor blue compact dwarf galaxy, by Papaderos et al. (2006) and the HIIRs in JKB 18 in the analysis by James et al. (2020). However, the
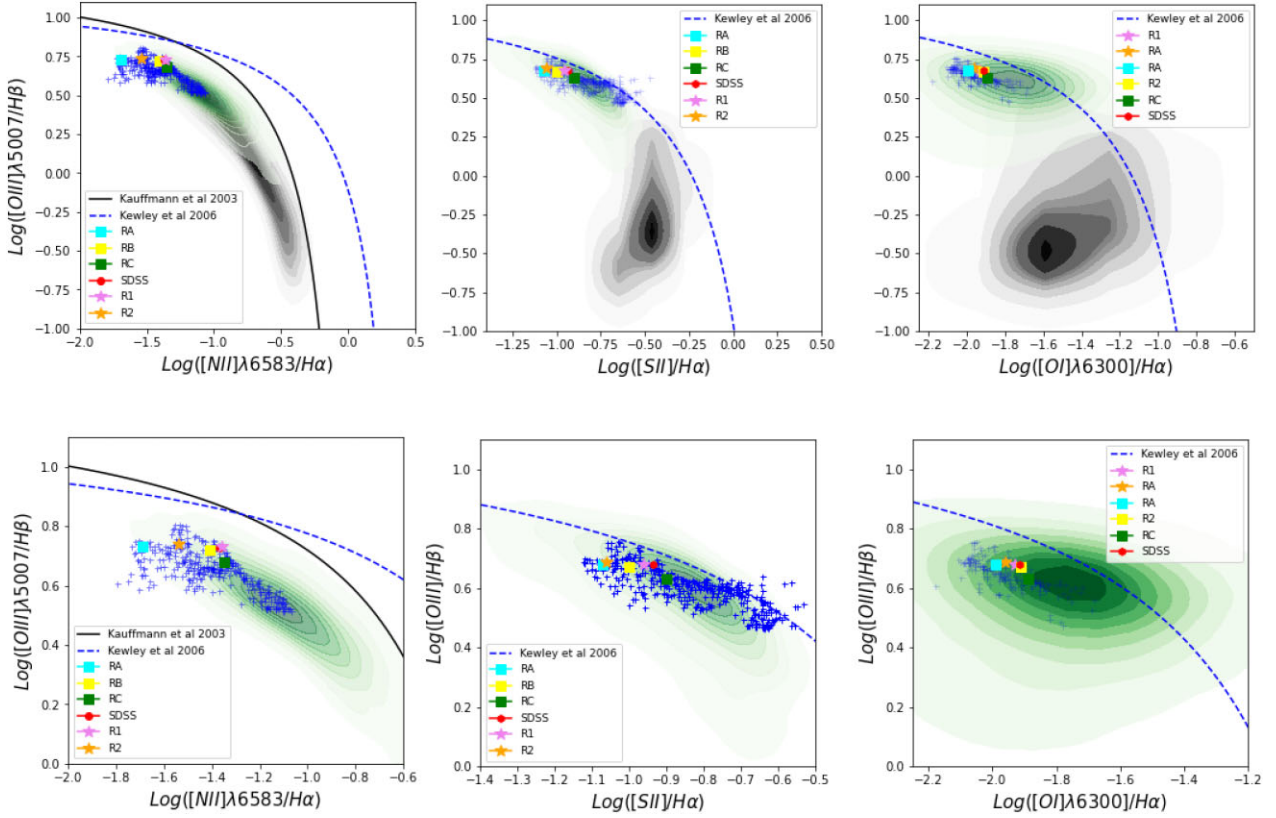
Figure 8. BPT diagnostic diagrams for J0842+1150. From left to right [O III] λ5007/Hβ versus [N II] λ6583/Hα, [S II] λ6717, 31/Hα, and [O I] λ6300/Hα in log scale. Only fluxes with S/N ≥ 4 are shown (blue cross). The red circle marks an individual fibre from SDSS. The black curve in the [N II] λ6584/Hα diagram represents the demarcation between star-forming galaxies (below and to the left of the curve) and AGN defined by Kauffmann et al. (2003). The blue–dashed line, in all three panels, is the theoretical demarcation limit from Kewley et al. (2006), that separates objects where the gas ionization is mainly due to hot massive stars (below and to the left of the curve) from those where other ionizing mechanism is required. The stars: violet and orange show the integrated region R1 and region R2, respectively. The squares: cyan, yellow, and green represent the integrated regions labelled as RA, RB, RC, respectively [see Appendix A (Supplementary Material)]. Density contours come from local SDSS star-forming galaxies (DR16) separated by EW(Hβ) ∼ 50 Å. Green contours for EW(Hβ) ≥ 50 Å and black for EW(Hβ) < 50 Å. The bottom row shows a zoom to the region of high ionization and low metallicity (see the description in the text).
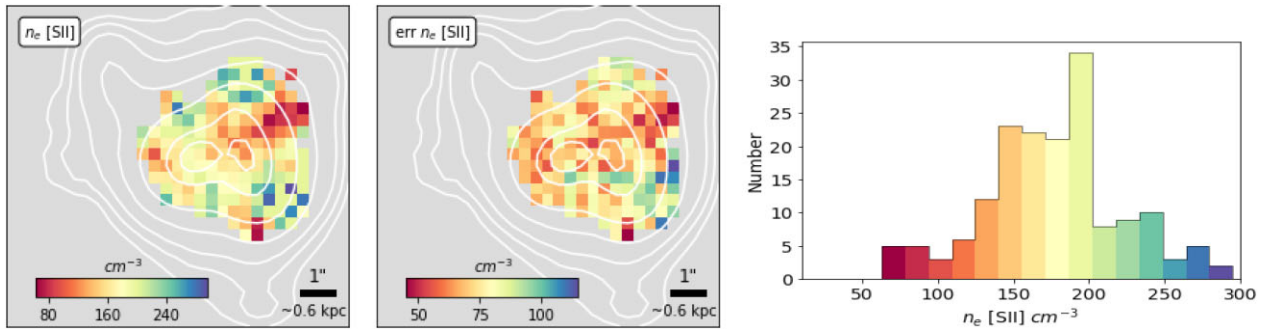
Figure 9. Derived electron density using the [S II] λ6717/λ6731 ratio. From left to right: density map, its error, and distribution across the nebula.

high temperatures found in these extreme galaxies are more related to their very low metallicity.

In our case, there is no evidence of higher temperatures due to shocks or other mechanism and the variations are similar to those found by Kumari et al. (2019) in the blue compact dwarf galaxy SBS 1415+437 between 11900 and 16300 K. Comparing individual galaxies with similar metallicities observed with long slit (e.g. Fernández et al. 2018), the results for the individual spaxels of J084220 in terms of metallicity and temperature are consistent.

6 ABUNDANCE DERIVATION USING THE DIRECT METHOD

The metallicity of HIIGs is an important parameter in order to characterize their evolutionary stage and to link them to other objects that present similar properties, e.g. dwarf irregulars or low surface brightness galaxies. Oxygen is the most abundant of the metals in GHIIRs. Additionally, carbon and nitrogen are among the most abundant chemical elements in star-forming galaxies. Since metals are a direct product of star formation in galaxies, chemical
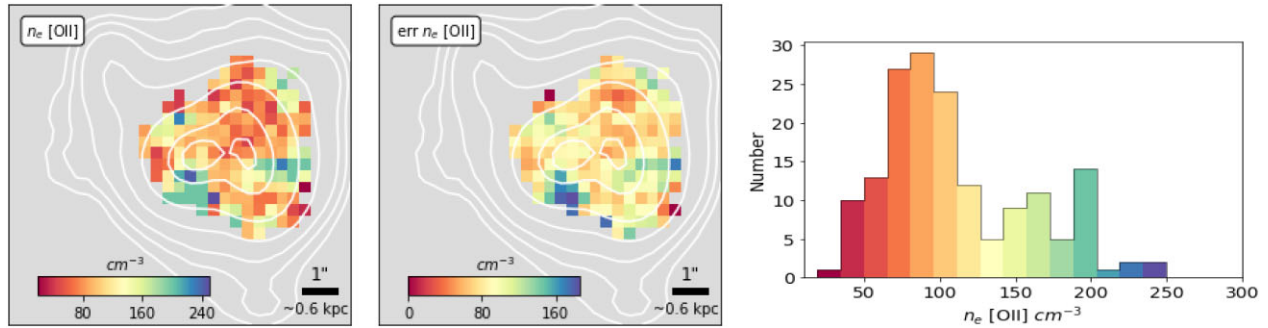
Figure 10. Derived electron density using [O II] λ3729/λ3726 ratio. From left to right: density map, its error and the distribution across the nebula.
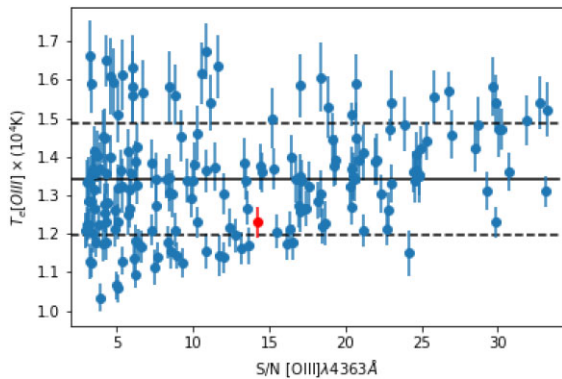

Figure 11. T_e[O III] derived directly from the measurement of the [O III] λ4363 line flux versus the relative error of the measurement. The solid horizontal line marks the mean value for T_e[O III] $\sim 1.33 \times 10^4$ K. The dashed lines represent $\pm 1\sigma$. The red circle is the value derived from the SDSS spectra using the same routine of PYNEB and corresponds to $1.23 \pm 0.03 \times 10^4$ K.

abundances are a powerful probe of the feedback processes driving their evolution. Oxygen occupies a key role in this type of study since its gas phase abundance can be inferred from strong nebular lines easily observed in the optical wavelength range in the low redshift Universe. In this section, we derive and discuss the helium, oxygen, and nitrogen abundances and the relation between them.

6.1 Ionic helium abundance

Helium is the second most common chemical species in the Universe. The study of helium abundance has the potential to unscramble

the chemical evolution within galaxies. The helium abundance is frequently derived using several emission lines in the optical and NIR wavelength ranges (e.g Kunth & Sargent 1983; Pagel et al. 1992; Masegosa, Moles & Campos-Aguilar 1994; Olofsson 1995; Izotov, Thuan & Guseva 2014; Fernández et al. 2018; Valerdi et al. 2019, particularly for primordial He determinations).

To determine the helium abundance, we use PYNEB for each spaxel with detected helium lines and estimate He$^+$/H$^+$; the adopted value is the weighted mean. In Fig. 14, we show the maps for He I λ3889, λ4471, λ4922, and λ6678. Given that He I λ3889 cannot be deblended from HI H8 λ3889.064 with our spectral resolution and He I λ4922 is very weak and only detected in some spaxels and with large uncertainty, we used just He I λ4471 and He I λ6678 to compute the helium abundance assuming the derived n_e and T_e[O III] for each spaxel. We use the effective recombination coefficients by Storey & Hummer (1995) for H and by Porter et al. (2012, 2013) for He which include collisional effects. The derived helium abundance for J084220 is in good agreement with values derived for H II galaxies with similar properties (e.g. Fernández et al. 2018) and Giant H II regions in local galaxies presented by Valerdi et al. (2021) although our results present larger errors.

Fig. 15 shows the helium abundance (He$^+$/H$^+$) distribution. For the integrated nebular region, we found a value of $12 + \log$ (He$^+$/H$^+$) $= 10.84 \pm 0.03$, and for regions R1 and R2, 10.81 ± 0.03 and 10.79 ± 0.03, respectively.

6.2 Oxygen abundance

Oxygen abundance in HIIGs ranges between $7.1 \leq 12 + \log$ (O/H) ≤ 8.3, obtained for more than 100 HIIGs with good quality data (Pérez-Montero & Díaz 2003). More recently Chávez et al. (2014),
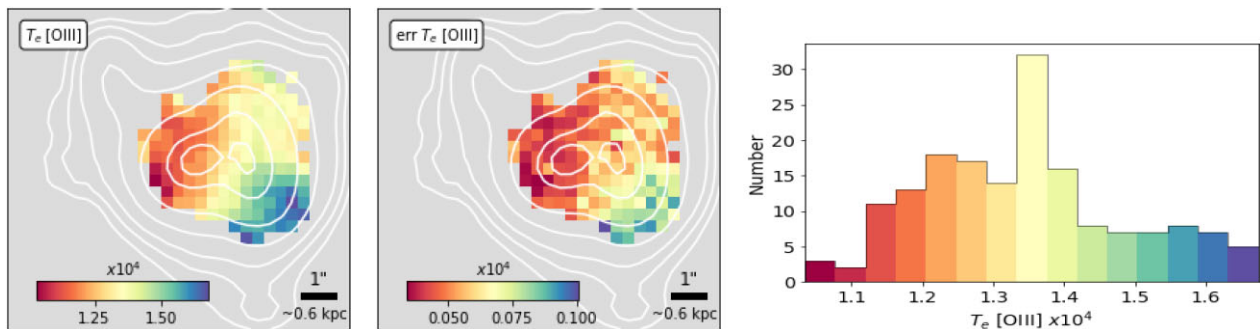

Figure 12. Derived electron temperature using [O III] λ4363/λ5007 (T_e[O III]) and n_e[S II]. From left to right: T_e map derived only for spaxels with fluxes in [O III] λ4363 ≥ 4. Error in the T_e[O III] map and distribution across the nebula.

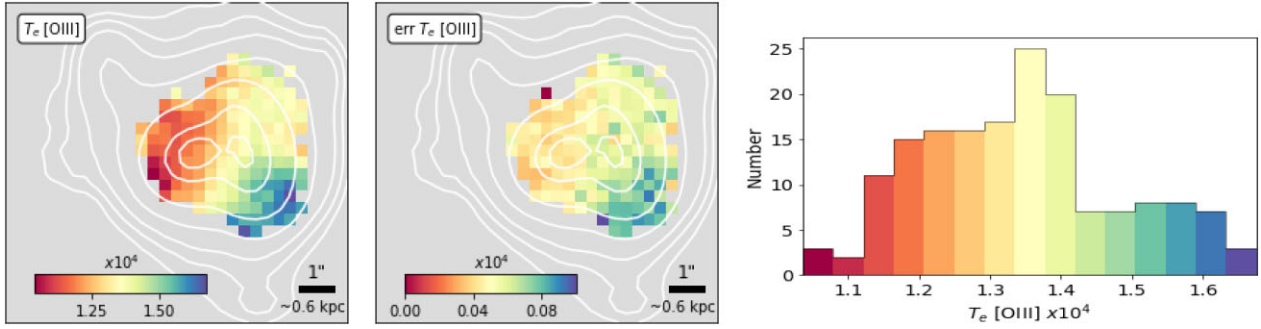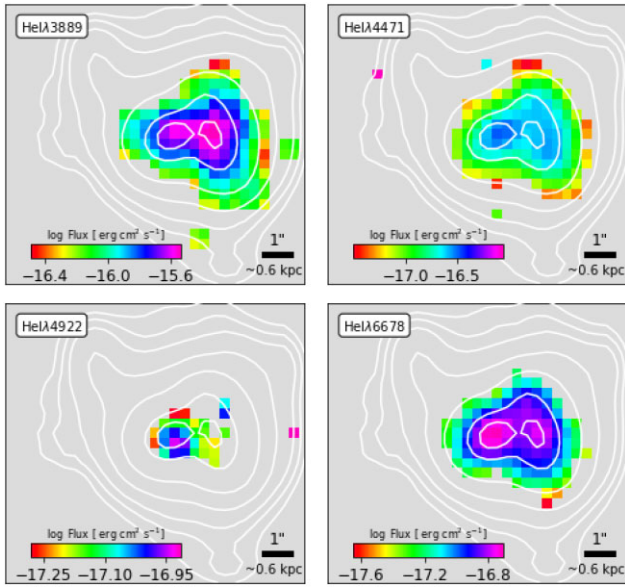**Figure 13.** Derived electron temperature using [O III] λ4363/λ5007 ($T_{\rm e}$[O III]) and $n_{\rm e}$[O II]. From left to righ: $T_{\rm e}$ map derived only for spaxels with fluxes in [O III] λ4363 ≥ 4, error in the $T_{\rm e}$[O III] map and distribution across the nebula.

Figure 14. Maps of λ3889, λ4471, λ4922, and λ4922 for spaxels with S/N > 4. H α isocontours are overlaid.

using a sample of 100 HIIGs between redshifts 0.02 and 0.2, found a median value of $12 + \log{\rm (O/H)} = 8.08$.

Here we calculate the ionic abundances of O^+/H^+ and O^{++}/H^+ using the line intensities of [O II] λλ3726, 29 and [O III] λλ4959, 5007, respectively, and the corresponding electron temperature and density $T_{\rm e}$[O III] and $n_{\rm e}$[S II]. These parameters can be used simultaneously in the `getIonAbundance` task in PYNEB to obtain ionic abundances. For the low ionization region, we have used the temperature relation proposed by Esteban et al. (2009) (equation 3) to estimate $T_{\rm e}$[O II] which is valid for a temperature range between 2000 and 18000 K. Finally, by adding the contribution of O^+/H^+ and O^{++}/H^+, we determine the total oxygen abundances as O/H = $O^+/H^+ + O^{++}/H^+$.

The spatial distribution of the derived $12 + \log{(O^+/H^+)}$, $12 + \log{(O^{++}/H^+)}$, and $12 + \log{\rm (O/H)}$ are displayed in Fig. 16. We also present the error map and the histogram distribution for each one.

We find an average value of $12 + \log{\rm (O/H)} = 8.06 \pm 0.06$, and a difference of $\Delta{\rm O/H} = 0.72$ dex between the minimum and maximum values (7.69 ± 0.06 and 8.42 ± 0.05) indicating a large metallicity range, unusual in a dwarf star-forming galaxy. A similarly large range has been reported in a recent paper for Haro 11 (Menacho et al. 2021).

6.3 Nitrogen abundance

In the optical, the nitrogen abundance is commonly derived from the [N II] λλ6548,83 lines. Our spectral resolution is enough to discriminate both lines from H α. We assume $T_{\rm e}$([N II]) = $T_{\rm e}$([O II]). We used the atomic data of Froese Fischer & Tachiev (2004) and collision strengths from Tayal (2011). For all spaxels, we assumed that N/H≈N^+/H^+ and thus we derive the total abundance of nitrogen.

Fig. 17 displays the nitrogen abundance map, the associated error, and the distribution across the galaxy. We found a mean value of $\log{\rm (N/H)}$ of -6.0, with a range between -6.4 and -5.4 and errors around 0.035 dex.

6.4 Nitrogen to oxygen abundance ratio

Nitrogen is mainly produced during the CNO cycle. In order to reproduce the tendency of N/O versus O/H in star-forming galaxies, nitrogen production has been interpreted due to two main sources. The first one is short-lived massive stars that produce pure 'primary' nitrogen and are responsible for the N/O ratio in a low-metallicity plateau. The second mechanism refers to the low- and intermediate-mass stars, which produce both secondary and primary nitrogen and enrich the ISM with a time delay relative to massive stars, and cause the increase of the N/O ratio and of the metallicity. In fact, secondary nitrogen becomes dominant and the nitrogen abundance increases at a faster rate than oxygen (Matteucci 1986; Henry, Edmunds & Köppen 2000; Thuan, Pilyugin & Zinchenko 2010; Wu & Zhang 2013; Vincenzo et al. 2016).

Strong nebular lines in the optical range allow reliable measurement of the (N/O) abundance ratio in star-forming galaxies, when both the [O II] λλ3727, 29 and [N II] λλ6548, 83 lines are available. Using the abundances as derived in Sections 6.2 and 6.3, we constructed the maps and histogram of log N/O as can be seen in Fig. 18. The values range between -1.7 and -1.30 throughout the galaxy.

Fig. 19 displays spaxel by spaxel on the plane N/O versus O/H; for comparison, we also plotted the star-forming galaxies from Izotov et al. (2006), with their nitrogen and oxygen abundances determined using the direct method. The average of log (N/O) in this sample is -1.45 ± 0.04. Interestingly, these galaxies have EW(H β) > 30 Å, which can be considered as a criterion to choose star-forming galaxies in the zone of high ionization and low metallicity in the BPT diagram (Telles & Melnick 2018).

The location of the spaxels and of the integrated regions is consistent with the location of the so called low metallicity plateau with an average log (N/O) = -1.52 ± 0.09, where nitrogen production is considered primary. For the integrated regions, we can also see
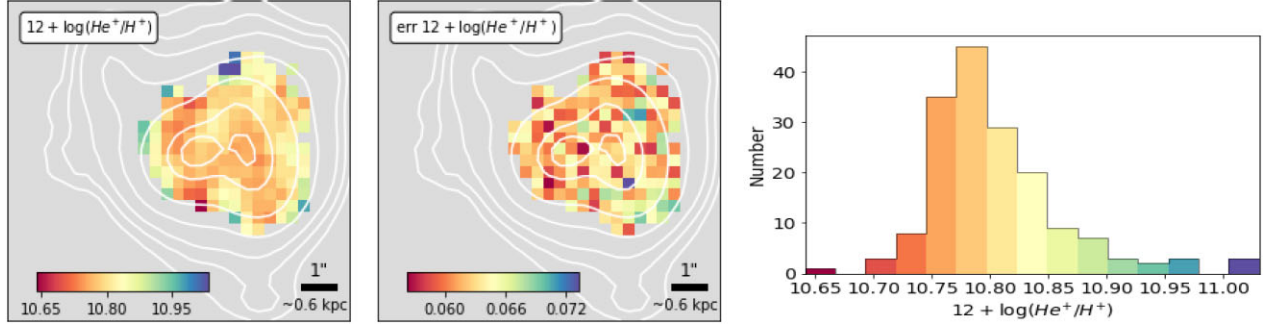
Figure 15. Left: helium abundance map, assuming T_e[O III] to quantify He$^+$/H$^+$. Centre and right: errors map and histogram of the distribution. The contours correspond to the Hα flux.
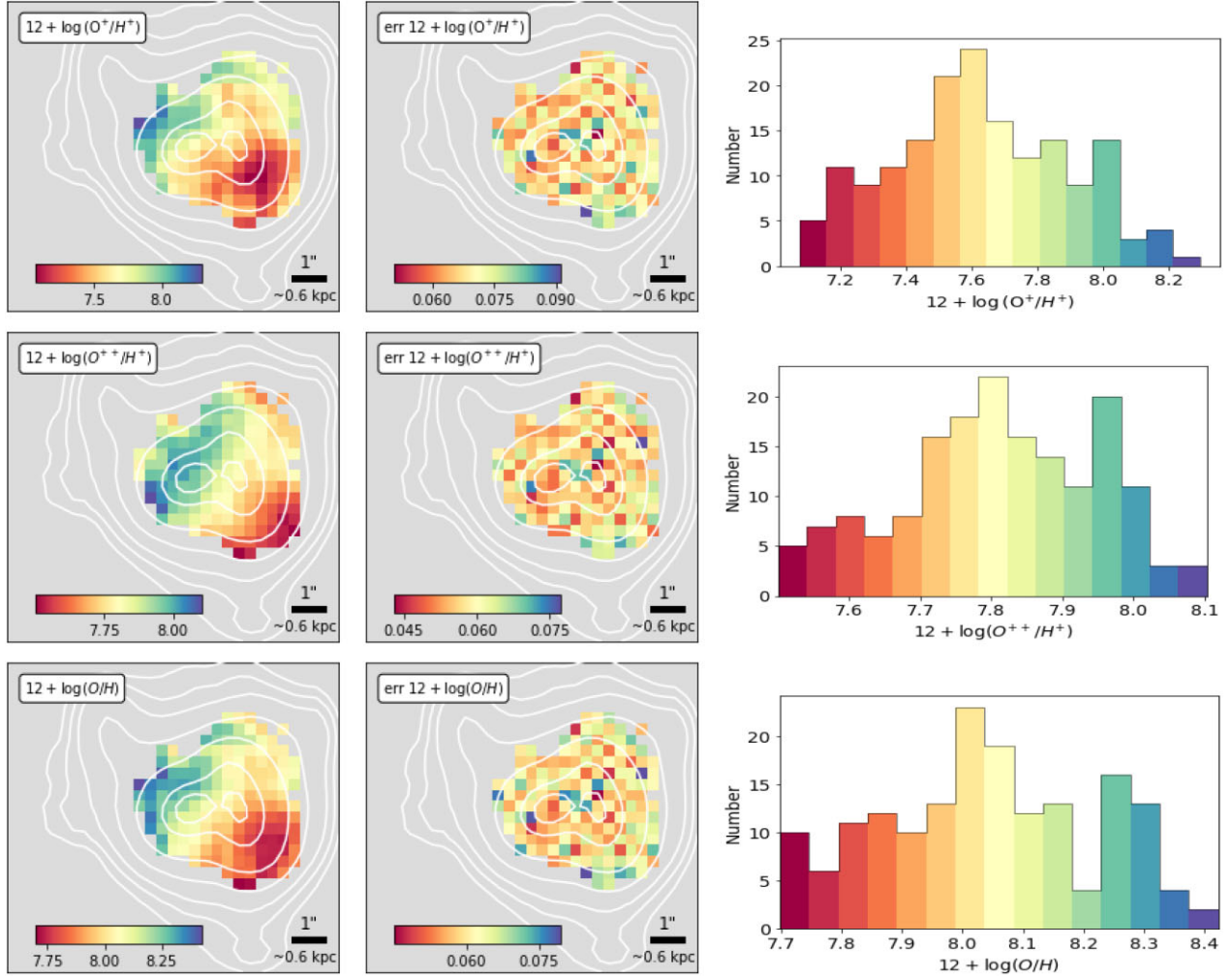

Figure 16. From top to bottom: Map of ionic and total oxygen abundance derived for $12 + \log(\text{O}^+/\text{H}^+)$, $12 + \log(\text{O}^{++}/\text{H}^+)$, and $12 + \log(\text{O}/\text{H})$ only for spaxels with derived T_e[O III]. Centre and right: corresponding errors and histograms of the abundance distribution.

a slight increase in the abundance of $\log(\text{N/O})$ with increase in metallicity, but still within the low-metallicity plateau for GHIIRs in nearby galaxies and HIIGs (Pérez-Montero & Contini 2009; Pilyugin et al. 2012; Andrews & Martini 2013). In general, we find that both for individual spaxels and for integrated regions the location of the points in the plane N/O versus O/H correspond to primary nitrogen.

7 EMPIRICAL ABUNDANCES

7.1 Oxygen abundance

As metallicity increases in low excitation photoionized regions, T_e cannot be determined due to the weakness (or absence) of the relevant auroral lines (e.g. [O III] λ4363 Å) and abundances cannot be directly derived. For these cases, empirical methods using strong forbidden
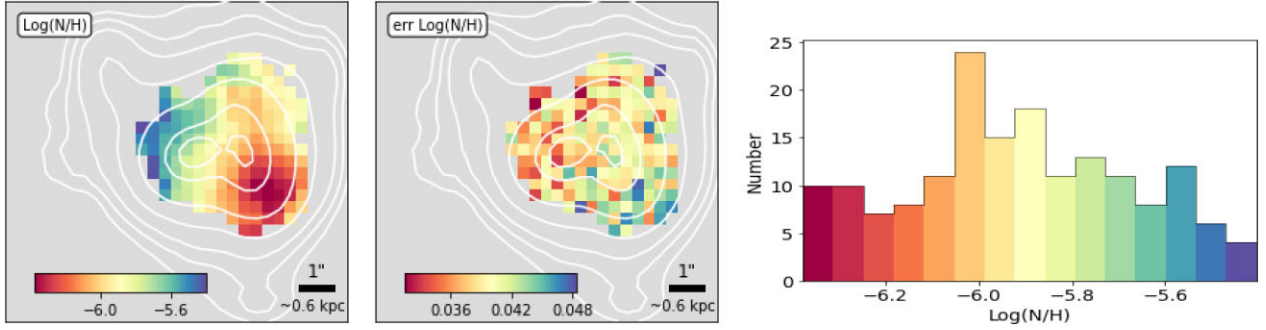
Figure 17. Nitrogen abundance map assuming $T_e[\text{N\,II}] = T_e[\text{O\,II}]$. Centre and right: distribution of the corresponding errors and histograms of the distribution.
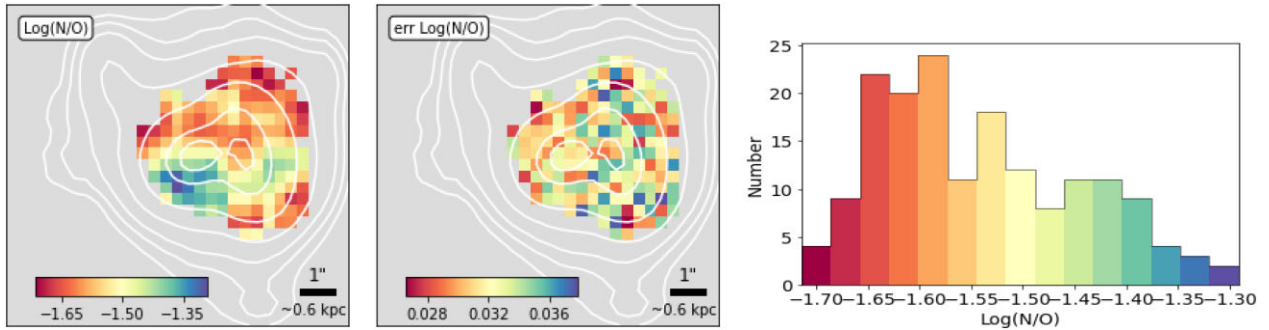

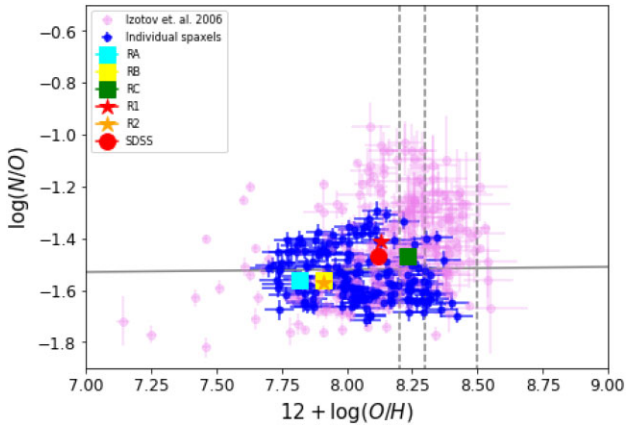**Figure 18.** log N/O map. Centre and right: corresponding errors and histograms of the distribution.

Figure 19. Individual spaxels in blue and integrated regions (stars and squares) in the plane log (N/O) versus $12 + \log(\text{O/H})$. A sample of extremely metal-poor emission-line galaxies from Izotov et al. (2006) are plotted as pink dots for comparison. The grey–dashed lines represent the transition metallicity $12 + \log(\text{O/H})$ reported by different works, Andrews & Martini (2013), Henry & Worthey (1999), Pilyugin et al. (2012), corresponding to 8.5, 8.3, and 8.2, respectively. The horizontal line is the average value for all spaxels.

lines have been proposed and calibrated over the years (e.g Searle 1971; Jensen, Strom & Strom 1976; Pagel et al. 1978, 1979; Shields & Searle 1978; Alloin et al. 1979; Díaz & Pérez-Montero 2000; Denicoló, Terlevich & Terlevich 2002; Kewley & Dopita 2002; Marino et al. 2013; Pettini & Pagel 2004). Some of these methods (O3N2, N2) have been more recently reviewed by Marino et al. (2013), Arellano-Córdova et al. (2016), and Pérez-Montero et al. (2021), this latter following the direct method in the ranges $7.7 <$

$12 + \log(\text{O/H}) < 8.6$, with a sample of 1969 extreme emission-line galaxies at a redshift $0 \leq z \leq 0.49$, selected from the SDSS.

Nowadays, O3N2 and N2 are the most widely used indicators of the oxygen abundance in photoionized regions. The line ratios that define these empirical parameters are given below. They are used both at low and high redshifts. N2 is defined as the ratio between two emission lines that are so close in wavelength that the parameter is not affected by reddening and calibration effects. The lines are also accessible in the near-infrared at moderate-to-high redshifts. O3N2 is only weakly affected by differential extinction and makes use of the strongest and most easily accessible emission lines in rest-frame optical spectroscopy.

Additionally, the relationship between N2 and O/H is mono-valued and although it is affected by the ionization parameter of the gas (e.g. Denicoló et al. 2002; Marino et al. 2013), it can be used to rank abundances in more extended regions, particularly relevant for integral field spectroscopy (IFS) data (e.g. López-Sánchez et al. 2011; Kehrig et al. 2013). O/H can also be derived using the ratio between [O II] and [O III] forbidden emission lines. This ratio is mostly sensitive to the ionization parameter and to the equivalent effective temperature of the ionizing stars, but it can also give an estimate of the total oxygen abundance based on the relation between stellar metallicity (Z) and the ionization parameter (log U) (Pérez-Montero et al. 2021).

To test whether strong line methods can be used to find metallicity variations across the nebula, we compared the metallicity spaxel by spaxel derived via the direct method [based on $T_e([\text{O\,III}] \lambda 4363/[\text{O\,III}] \lambda\lambda 4959, 5007]$ with that obtained with empirical methods such as N2 (with the calibrations by Raimann et al. 2000; Denicoló et al. 2002; Pettini & Pagel 2004; Pérez-Montero & Contini 2009; Pérez-Montero et al. 2021), O3N2 (Pettini & Pagel 2004; Nagao, Maiolino & Marconi 2006; Pérez-Montero & Contini 2009; Pérez-Montero et al. 2021), and O32 (Pérez-Montero et al. 2021).
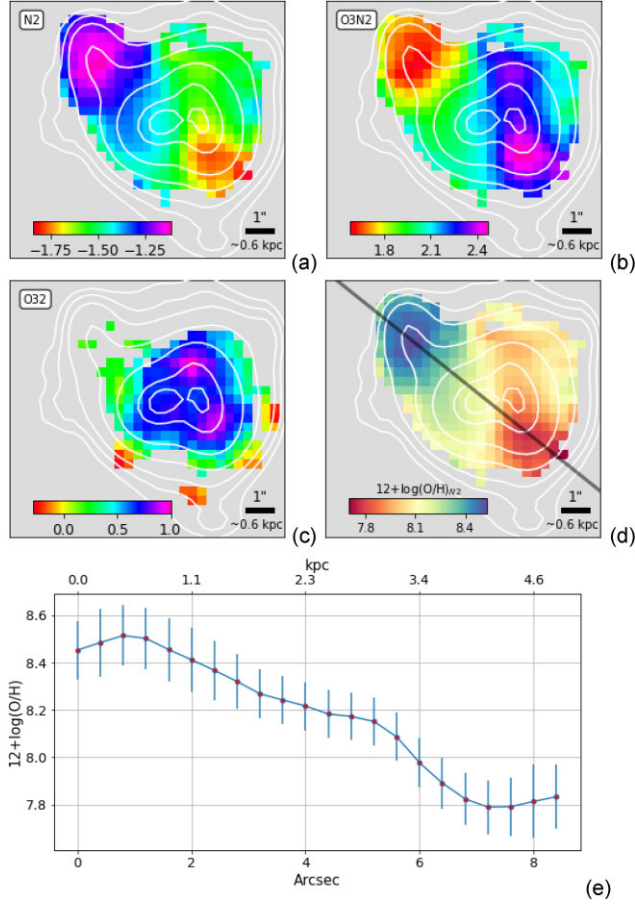
Figure 20. (a,b,c): Maps of the line ratios N2, O3N2, and O32 defined in the text. (d) oxygen abundance map derived from the strong line method (N2); the black line indicates the maximum metallicity variation. (e): oxygen abundances traced along the line of maximum metallicity variation drawn in panel (d).

We use the following line ratios to derive the empirical oxygen abundance:

$$N2 = \log\left(\frac{I([N\,II]\lambda 6583)}{I(H\alpha)}\right) \tag{3}$$

$$O3N2 = \log\left(\frac{I([O\,III]\lambda 5007)}{I(H\beta)}\frac{I(H\alpha)}{I([N\,II]\lambda 6583)}\right) \tag{4}$$

$$O32 = \log\left(\frac{I([O\,III]\lambda 4959, 5007)}{I([O\,II]\lambda 3727)}\right) \tag{5}$$

These line ratios maps are shown in Fig. 20. Fig. 21 shows N2, O3N2, and O32 for the spaxels with oxygen abundances derived by the direct method. For comparison, we included Pettini & Pagel (2004), Marino et al. (2013), Pérez-Montero et al. (2021) calibrations for N2. They agree within the errors. For values greater than −1.5 and 12 + log (O/H) > 8, the results fall in Pettini & Pagel (2004) calibration. Our spaxel by spaxel results for J0842+1150 give a relation 12 + log (O/H) = 9.80 + 1.12 × N2 with an rms of 0.21. Following this relation, it is possible to estimate the metallicity over a larger number of spaxels.

For the O3N2 indicator, we also included Nagao et al. (2006) calibration, an approximation by a third degree polynomial function. For individual spaxels, we find consistency between different calibrations in the range of O3N2 of ∼−1.3 and −1.8 and 12 +
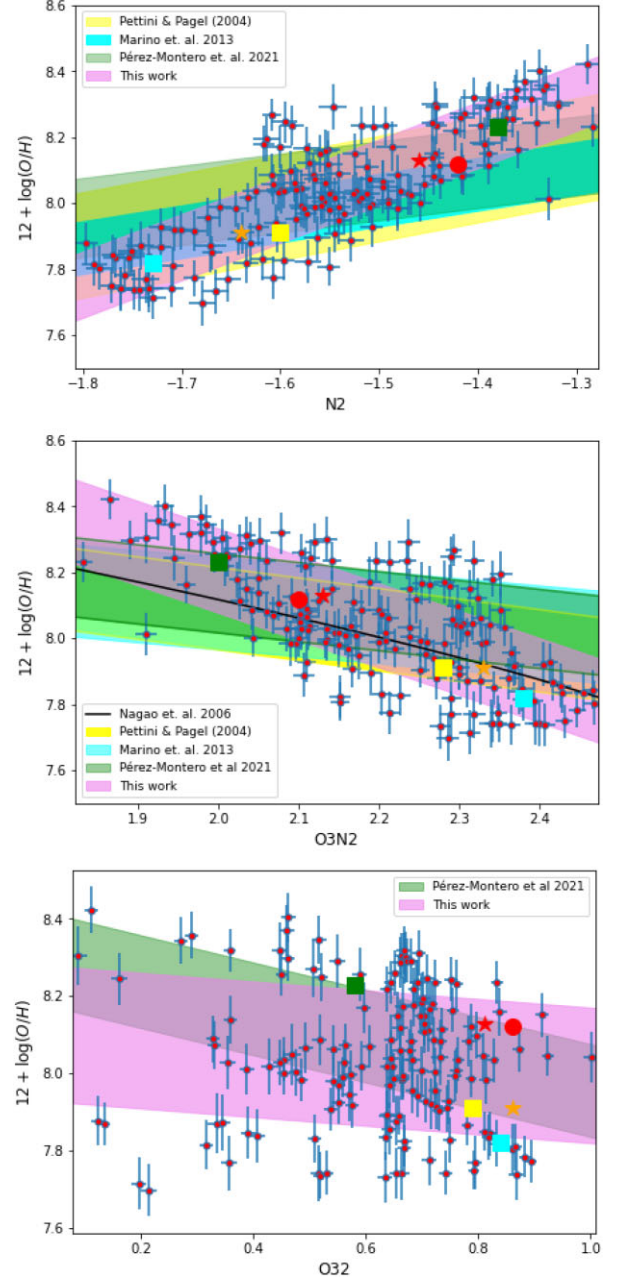

Figure 21. N2, O3N2, and O32 versus 12 + log (O/H). The symbols correspond to the integrated regions as described in Fig. 8. The coloured regions correspond to different calibrations found in the literature as described in the text. The violet region in the three plots corresponds to the linear fits using the spaxels (small red circles) and its rms; errors in both axes have been considered for the fits.

log (O/H) between 8.1 and 8.4. Outside this range, our results are more consistent with Nagao et al. (2006) calibration.

The resulting fittings for O3N2 and O32 are: 12 + log (O/H) = 9.86 − 0.83 × O3N2 and 12 + log (O/H) = 8.10 − 0.21 × O32 with an rms of 0.12 and 0.17 dex, respectively. The largest discrepancies are found in O32; consistent with Pérez-Montero et al. (2021) who have found that the correlation between O32 and metallicity for metal-poor galaxies is not very strong.

In general, our results for individual spaxels are consistent with the integrated calibrators presented in the literature. This shows that it is
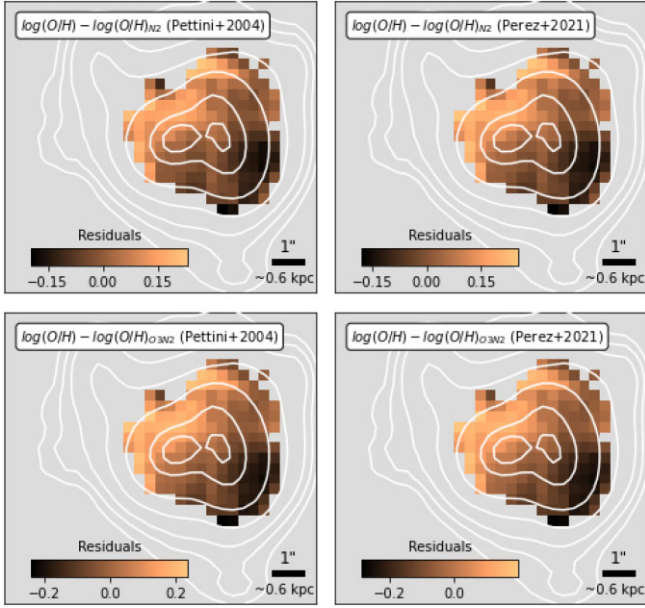
Figure 22. Oxygen abundance difference between the direct method and strong-line methods. This variation is around 0.2 dex in the N2 calibrator and 0.25 dex for the O3N2 in the regions of high and low temperatures. The variations are similar whether using the N2 or O3N2 calibrators from Pettini & Pagel (2004) or Pérez-Montero et al. (2021).

still possible to obtain a good determination of abundances and find gradients based on strong line methods for IFS observations where it is not possible to derive electron temperature, especially using the calibrators for N2 and O3N2 that have lower dispersion and provide the tightest correlations.

Fig. 22 shows the differences in the oxygen abundances derived from the direct method, which has a tight dependence on the temperature, and the strong-line method which uses strong line ratios only. In most spaxels in between the bursts of star formation, we derive consistent values. However, we find differences of 0.2 dex in the results of individual spaxels for ratios at low and high N2 and O3N2, corresponding to the most extreme temperatures found in the galaxy around ∼11000 and ∼16000 K.

The strong line methods are secondary calibrated methods that could be degenerate with respect to some properties of the nebula like pressure and ionization parameter, therefore give imprecise values in the high and low abundance ends and fail to probe the diverse conditions in one galaxy, especially for IFU observations. Nevertheless, they still represent a powerful tool to estimate the abundances in absence of weak lines to measure temperatures (Dopita et al. 2013). Although we can not find a direct explanation for those differences, we suggest that part of these discrepancies could be originated from a temperature effect and that additional bias could be related to the atomic data used in the empirical derivations, compared with the set used here (e.g Pérez-Montero et al. 2021). Similar results and conclusions have been found by Menacho et al. (2021).

7.2 Strong-line methods and the nitrogen-to-oxygen abundance ratio

N/O can be derived using a combination of strong collisional lines in the form of the N2O2 parameter Pérez-Montero & Contini (2009). A problem though is that the lines used have a significant wavelength difference which renders the parameter more sensitive to
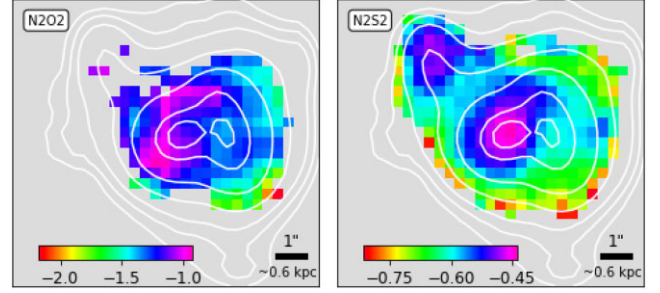

Figure 23. N2O2 (left) and N2S2 (right) maps. Hα isocontours are overlaid.

observational issues, like calibration errors or the fact that a single observing set-up may not yield all the relevant lines simultaneously. Therefore, Pérez-Montero & Contini (2009) also suggest the use of N2S2 to characterize the abundance ratio between nitrogen and oxygen. These indicators are given by:

$$N2O2 = \log\left(\frac{I([\text{N\,II}]\lambda 6583)}{I([\text{O\,II}]\lambda 3727)}\right) \quad (6)$$

$$N2S2 = \log\left(\frac{I([\text{N\,II}]\lambda 6583)}{I([\text{S\,II}]\lambda 6717, 6731)}\right) \quad (7)$$

Maps of N2O2 and N2S2 are shown in Fig. 23. It can be noticed that N2S2 reaches farther than N2O2, towards the east of the galaxy.

A tight correlation was found by Pérez-Montero et al. (2021) between the above calibrators and N/O. The relations, given by: $\log(\text{N/O}) = -0.31 + 0.87 \times \text{N2O2}$ and $\log(\text{N/O}) = -1.005 + 0.857 \times \text{N2S2}$ are valid in the ranges $-1.7 < \text{N2O2} < -0.5$, and $-0.8 < \text{N2S2} < 0.3$, which correspond to $-1.8 < \log(\text{N/O}) < -0.75$ and $-1.7 < \log(\text{N/O}) < -0.75$, with standard deviation of 0.04 and 0.08 dex, respectively. These calibrations are plotted in Fig. 24, where we also show our relation between these parameters and the nitrogen-to-oxygen ratio as derived via the direct method both for the spaxels across the galaxy and for the chosen integrated regions.

Our data spaxels fit best Pérez-Montero et al. (2021) calibration for N2S2. For N2O2, the points depart from Pérez-Montero et al. (2021) fit. Our fits are: $\log(\text{N/O}) = -1.15 + 0.30 \times \text{N2O2}$ and $\log(\text{N/O}) = -1.15 + 0.64 \times \text{N2S2}$ with an rms of 0.089 and 0.085 dex, respectively.

Our spaxel by spaxel N2O2 values agree better with Strom et al. (2018) calibration for N/O derived for high-z star-forming galaxies than with Pérez-Montero et al. (2021). For N2S2 versus $\log(\text{N/O})$, the agreement of this work and derived local and high-z calibration by Pérez-Montero et al. (2021) and Strom et al. (2018), respectively are consistent within the errors.

8 CHEMICAL INHOMOGENEITIES IN HIIGS AND BCD

The oxygen abundance of the ionized gas in HIIGs has been found to be homogeneously distributed on spatial scales of >100 pc (e.g. Lagos et al. 2009; Cairós et al. 2009; Pérez-Montero & Contini 2009; García-Benito & Pérez-Montero 2012; Kehrig et al. 2016). It has to be said however, that the Hα distribution in some of the galaxies in these works, does not show multiple star-forming knots. In general, only weak gradients are observed on scales of hundreds of parsecs, e.g. IIZw70 in Kehrig et al. (2008) or Tol 0104−388 and Tol 2146−391 in Lagos et al. (2012).

The apparent homogeneous distribution of abundances in HIIGs may be due to the fact that the newly synthesized elements were rapidly dispersed on time-scales $<10^7$ yr and mixed in the ISM.
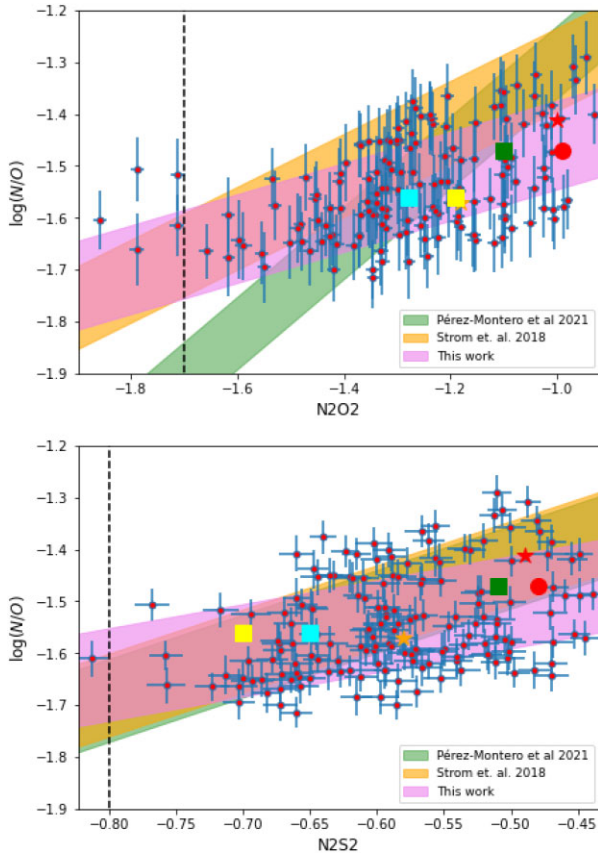
Figure 24. Relation between log (N/O), as derived following the direct method, and the parameters N2O2 and N2S2 for the individual spaxels and for the integrated regions; the vertical–dashed lines show the lowest value for the calibrations to be valid. The region in green corresponds to Pérez-Montero et al. (2021) calibration whereas the region in yellow is derived from Strom et al. (2018) using high-z star-forming galaxies; in violet is shown the fit for the spaxels in this work. The large solid points represent the different integrated regions as described in the text.

Processes associated with massive star formation are extremely efficient at mixing hot and warm ionized gas. This hypothesis requires that the metals be ejected and mixed homogeneously within the ISM during the H II region lifetime to ensure the mixing of individual clouds (Roy & Kunth 1995; Kobulnicky & Skillman 1997).

A possible explanation for the homogeneous chemical appearance of HIIGs on spatial scales of >100 pc was proposed by Tenorio-Tagle, Munoz-Tunon & Cid-Fernandes (1996) in which the ejecta from stellar winds and SNe could undergo a long (∼100 Myr) cycle in a hot phase (∼10^6 K) before mixing with the surrounding ISM. Thus, the new metals processed and injected by the current star formation episode are possibly not observed and remain for longer in the hot gas phase, whereas the metals from previous events are well mixed and homogeneously distributed through the whole extent of the galaxy.

On the other hand, Lagos et al. (2009) for UM408 and Izotov et al. (2006) in SBS 0335−052E, using IFU observations find a variation of ∼0.5 dex in both galaxies and a common point is that the maximum oxygen abundance found does not correspond to the position of any of the identified bursts of star-formation. Similar variation is found in NGC 6822, a dwarf irregular galaxy in the local group, with an average of 12 + log (O/H) ∼ 8.15 (Lee, Skillman & Venn 2006).

James et al. (2020) present a summary of other dwarf galaxies, Haro 11, UM 448, NGC 4449, NGC 5253, and Mrk 996 among others, highlighting that chemical maps of (O/H) show differences of ∼0.5 dex. They conclude that the chemical inhomogeneities should be the result of outflows of metal-enriched gas due to SNe, the accretion of metal-poor gas due to interactions/mergers, self-enrichment from winds of massive stars, or bursts of star-formation at shorter times compared with the time-scale of metal mixing.

Finally, as discussed in Bresolin (2019), there are a handful of dwarf-irregular galaxies that actually have well-ordered gradients that are comparable to spiral galaxies. For example, NGC 6822, NGC 4449, DDO 68 each show a chemical abundance gradient, despite the absence of spiral structures, deemed necessary for gradients. This links the existence of these gradients to recent enhancements in their star-formation activity, where metal mixing time-scales are longer than the time between bursts of star-formation.

Analysing metal-poor galaxies, Sánchez Almeida et al. (2013), Sánchez Almeida et al. (2014), Sánchez Almeida et al. (2015), and Olmo-García et al. (2017) concluded that the observed metallicity inhomogeneities and gradients are only possible if the metal-poor gas fell onto the disc recently. Among several possibilities for the origin of the metal-poor gas, they favour the infall predicted by numerical models. Thus, if this interpretation is correct, metal-poor galaxies trace the cosmic web gas in their surroundings. Their results are consistent with assuming that the local galaxies characterized by a bright peripheral clump on a faint tail, are discs in the early stages of assembling, their star formation being sustained by accretion of external metal-poor gas.

The low metallicity found for J0842+1150 (20 per cent of solar) is consistent with it being a metal-poor galaxy. Normally, these galaxies have been morphologically identified as cometary or tadpoles, and this association between low metallicity and tadpole or cometary shapes suggests that those are attributes characteristic of very young systems (Sánchez Almeida et al. 2013). A possible formation scenario has been proposed for which the impacting gas clouds have the largest effect on the outskirts of galaxies where the ambient pressure and column density are low which, for most orientations of the galaxy, result in a cometary shape (Sánchez Almeida et al. 2015).

The existence of chemical inhomogeneities is particularly revealing because the time-scale for mixing in disc galaxies is short, of the order of a fraction of the rotational period. This implies that the metal-poor gas in such galaxies was recently accreted from a nearly pristine cloud, very much in line with the expected cosmic cold-flow accretion predicted to build disc galaxies (Olmo-García et al. 2017, and references therein). However, the fate of the metals released by massive stars in H II regions is still an open question, and the processes of metal dispersal and mixing are very difficult to model.

In Fig. 25, we show the image in *g* band from SDSS of J0482+1150, where the extremes of metal content are presented; the lowest metallicity region with a metal content of about 1/10th of Solar and the eastern extension, a linear structure, with the highest value of metallicity in the galaxy (using N2 calibrator), about half the Solar value. The high value of the metal content of the north-east structure and its shape suggest an outflow of enriched material.

A possible interpretation for the marked difference in oxygen abundance and starburst activity that we find could be that we are witnessing an ongoing interaction system triggering multiple star-forming regions localized in two dominant clumps of different metallicity. From the distribution of the equivalent width of Balmer lines (akin to age) the more symmetric cluster (R1) shows lower EW(Hβ) with an underlying tail or a cometary shape towards the
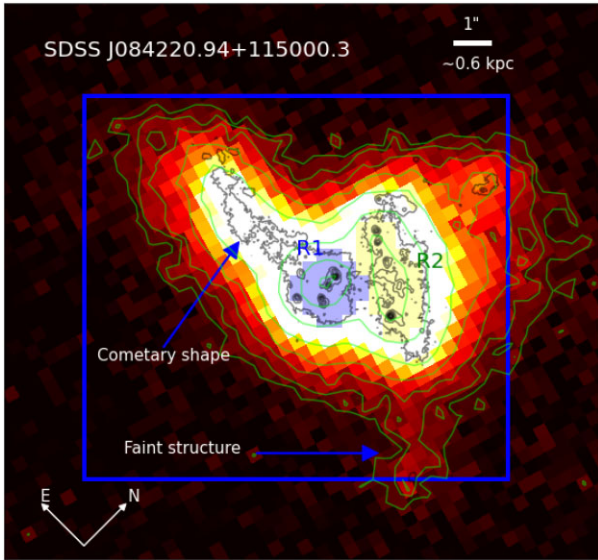
Figure 25. Broad-band SDSS image in *g* band. The main star-forming regions are indicated: region R1 in blue, region R2 in yellow, a very faint tail feature can be identified towards the south-west of region R2 and a cometary shape to the east of region R1. Isocontours of *g* band from SDSS are shown in green, whereas in black are shown isocontours of the WFC3 UVIS2 F336W from *HST* between 4.55×10^{-20} and 1.5×10^{-18} erg cm^{-2}s^{-1} Å^{-1} corresponding to the minimum and maximum, respectively. The blue square is the FoV of MEGARA.

east, whereas the more elongated one (R2) shows larger EW(H β) and also the lowest metallicity.

Additionally, a very faint tail feature can be identified towards the south–west of region R2. Kinematic analysis of this data will allow us to look for signs of interaction in the rotation patterns. Briefly, the velocity field shows an apparent rotational motion with maximum velocity of 60 km s^{-1}, with a position angle of the kinematic axis, $\theta_{\rm kin} = 124 \pm 9$, as determined by a tilted-ring analysis of the emission lines velocity field based on a kinemetry method developed by Krajnović et al. (2006). However, these rotation motions look disturbed, perhaps as a consequence of multiplicity of star forming regions or merger systems. Towards region #1, the velocity field appears blue-shifted with velocity between -5 and -15 km s^{-1} whereas region #2, more elongated, shows two velocity components: one about 15 km s^{-1} and another between 30–35 km s^{-1}. The zero velocity is defined in the intermediate region between regions #1 and #2. A detailed analysis will be presented in a forthcoming paper (Fernández-Arenas et al. in prep).

9 SUMMARY AND CONCLUSIONS

In this work, we present MEGARA IFU spectroscopy of the metal-poor galaxy J0842+1150. We derived the distribution of physical properties across the FoV of MEGARA and integrated properties for the galaxy as a whole and for individual star-forming regions.

The resolution spatial coverage and high quality of data of MEGARA IFU allowed the detection in a large number of spaxels of the auroral forbidden emission line [O III] λ4363 with a signal-to-noise level S/N $> 4\sigma$. The spaxels with detection of [O III] λ4363 include the main star-forming regions and their surrounding area allowing the mapping of the metal distribution in J0842+1150 using the direct method.

(i) Our main result is the detection of an unusually large metallicity range in a dwarf star-forming galaxy. The distribution of oxygen abundance, computed using the direct method, has a mean value of $12 + \log{(O/H)} = 8.03 \pm 0.06$ and a range of $\Delta(O/H) = 0.72$ dex between the minimum 7.69 ± 0.06 and maximum 8.42 ± 0.05 values. This range implies a metallicity span of a factor of 5 over a spatial extent of ~ 1 kpc.

(ii) We find that for both individual spaxels and integrated regions, the location of the points in the diagram N/O versus O/H corresponds to primary nitrogen with similar location to metal-poor galaxies reported in the literature.

(iii) The analysis of the emission line ratios and BPT diagrams discard the presence of any AGN activity or shocks as the ionization source in this galaxy.

(iv) The comparison of the strong-line methods to derive oxygen and nitrogen abundances for individual spaxels and integrated region are in general in agreement within the errors with the calibrations reported in the literature specially the N2 and O3N2 tracers of oxygen abundance and N2S2 for the ratio of N/O. This supports the use of strong-lines methods and calibrations for spatially resolved IFS data wherein many cases, the detection of weak emission lines is not possible.

(v) The integrated values derived in this work for the physical properties of J0842+1150, such as abundances and global velocity dispersion are in agreement with values previously derived in the literature with long-slit or fibre spectroscopy.

(vi) Among the possible mechanisms to explain the starburst activity and the large variation of oxygen abundance in this galaxy, our data support a possible scenario where we are witnessing an ongoing interaction of very young systems. A detailed multicomponent kinematic analysis will be presented in a forthcoming paper (Fernández-Arenas et. al. in preparation).

The study of HIIGs can offer detailed insight into processes that might depend on metallicity and that could have played an important role in the early evolution of galaxies. We plan to extend this project to objects similar to J08422+1150 (selected from Chávez et al. 2014). We hope to use also 3D spectroscopy which will allow us to map in detail their interstellar medium chemical abundances and possible inhomogeneities and to link them to other properties like the ionizing stellar fabric and morphology, and their kinematics.

DATA AVAILABILITY

The data underlying this article will be shared on reasonable request to the corresponding author.

REFERENCES

Alloin D., Collin-Souffrin S., Joly M., Vigroux L., 1979, A&A, 78, 200
Aloisi A. et al., 2007, ApJ, 667, L151
Amorín R., Pérez-Montero E., Vílchez J. M., Papaderos P., 2012, ApJ, 749, 185
Amorín R. et al., 2017, Nature Astron., 1, 0101
Andrews B. H., Martini P., 2013, ApJ, 765, 140
Annibali F. et al., 2013, AJ, 146, 144
Arellano-Córdova K. Z., Rodríguez M., Mayya Y. D., Rosa-González D., 2016, MNRAS, 455, 2627
Baldwin J. A., Phillips M. M., Terlevich R., 1981, PASP, 93, 5
Basu-Zych A. R. et al., 2009, ApJ, 699, L118
Bordalo V., Telles E., 2011, ApJ, 735, 52
Bosch G. et al., 2019, MNRAS, 489, 1787
Bresolin F., 2019, MNRAS, 488, 3826
Bresolin F. et al., 2020, MNRAS, 495, 4347
Brinchmann J., Kunth D., Durret F., 2008, A&A, 485, 657
Brorby M., Kaaret P., 2017, MNRAS, 470, 606
Brorby M., Kaaret P., Prestwich A., Mirabel I. F., 2016, MNRAS, 457, 4081
Cairós L. M., Caon N., Papaderos P., Kehrig C., Weilbacher P., Roth M. M., Zurita C., 2009, ApJ, 707, 1676
Campbell A., Terlevich R., Melnick J., 1986, MNRAS, 223, 811
Carrasco E. et al., 2022, MNRAS, 509, 6183
Chávez R., Terlevich E., Terlevich R., Plionis M., Bresolin F., Basilakos S., Melnick J., 2012, MNRAS, 425, L484
Chávez R., Terlevich R., Terlevich E., Bresolin F., Melnick J., Plionis M., Basilakos S., 2014, MNRAS, 442, 3565
Chávez R., Plionis M., Basilakos S., Terlevich R., Terlevich E., Melnick J., Bresolin F., González-Morán A. L., 2016, MNRAS, 462, 2431
Curti M. et al., 2022, MNRAS, 512, 4136
Denicoló G., Terlevich R., Terlevich E., 2002, MNRAS, 330, 69
Díaz A. I., Pérez-Montero E., 2000, MNRAS, 312, 130
Dopita M. A., Sutherland R. S., Nicholls D. C., Kewley L. J., Vogt F. P. A., 2013, ApJS, 208, 10
Esteban C., Peimbert M., 1995, A&A, 300, 78
Esteban C., Bresolin F., Peimbert M., García-Rojas J., Peimbert A., Mesa-Delgado A., 2009, ApJ, 700, 654
Esteban C., Bresolin F., García-Rojas J., Toribio San Cipriano L., 2020, MNRAS, 491, 2137
Fernández V., Terlevich E., Díaz A. I., Terlevich R., Rosales-Ortega F. F., 2018, MNRAS, 478, 5301
Froese Fischer C., Tachiev G., 2004, At. Data Nucl. Data Tables, 87, 1
García-Benito R., Pérez-Montero E., 2012, MNRAS, 423, 406
Gil de Paz A., Madore B. F., Pevunova O., 2003, ApJS, 147, 29
González-Morán A. L. et al., 2019, MNRAS, 487, 4669
González-Morán A. L. et al., 2021, MNRAS, 505, 1441
Gonçalves T. S. et al., 2010, ApJ, 724, 1373

Gordon K. D., Clayton G. C., Misselt K. A., Landolt A. U., Wolff M. J., 2003, ApJ, 594, 279
Grimes J. P. et al., 2007, ApJ, 668, 891
Groves B., Brinchmann J., Walcher C. J., 2012, MNRAS, 419, 1402
Hägele G. F., Díaz Á. I., Cardaci M. V., Terlevich E., Terlevich R., 2007, MNRAS, 378, 163
Hägele G. F., Díaz Á. I., Terlevich E., Terlevich R., Pérez-Montero E., Cardaci M. V., 2008, MNRAS, 383, 209
Henry R. B. C., Worthey G., 1999, PASP, 111, 919
Henry R. B. C., Edmunds M. G., Köppen J., 2000, in American Astronomical Society Meeting Abstracts. American Astronomical Society, United States, p. 76.08
Izotov Y. I., Stasińska G., Meynet G., Guseva N. G., Thuan T. X., 2006, A&A, 448, 955
Izotov Y. I., Thuan T. X., Guseva N. G., 2012, A&A, 546, A122
Izotov Y. I., Thuan T. X., Guseva N. G., 2014, MNRAS, 445, 778
James B. L., Kumari N., Emerick A., Koposov S. E., McQuinn K. B. W., Stark D. P., Belokurov V., Maiolino R., 2020, MNRAS, 495, 2564
Jensen E. B., Strom K. M., Strom S. E., 1976, ApJ, 209, 748
Kauffmann G. et al., 2003, MNRAS, 346, 1055
Kehrig C., Telles E., Cuisinier F., 2004, AJ, 128, 1141
Kehrig C., Vílchez J. M., Sánchez S. F., Telles E., Pérez-Montero E., Martín-Gordón D., 2008, A&A, 477, 813
Kehrig C. et al., 2013, MNRAS, 432, 2731
Kehrig C. et al., 2016, MNRAS, 459, 2992
Kehrig C., Vílchez J. M., Guerrero M. A., Iglesias-Páramo J., Hunt L. K., Duarte-Puertas S., Ramos-Larios G., 2018, MNRAS, 480, 1081
Kewley L. J., Dopita M. A., 2002, ApJS, 142, 35
Kewley L. J., Groves B., Kauffmann G., Heckman T., 2006, MNRAS, 372, 961
Kisielius R., Storey P. J., Ferland G. J., Keenan F. P., 2009, MNRAS, 397, 903
Kobulnicky C., Skillman E. D., 1997, in American Astronomical Society Meeting Abstracts. American Astronomical Society, United States, p. 76.03
Krajnović D., Cappellari M., de Zeeuw P. T., Copin Y., 2006, MNRAS, 366, 787
Kumari N., James B. L., Irwin M. J., Aloisi A., 2019, MNRAS, 485, 1103
Kunth D., Sargent W. L. W., 1983, ApJ, 273, 81
Kunth D., Östlin G., 2000, A&A Rev., 10, 1
Lagos P., Telles E., Muñoz-Tuñón C., Carrasco E. R., Cuisinier F., Tenorio-Tagle G., 2009, AJ, 137, 5068
Lagos P., Telles E., Nigoche Netro A., Carrasco E. R., 2012, MNRAS, 427, 740
Lee H., Skillman E. D., Venn K. A., 2006, ApJ, 642, 813
López-Sánchez Á. R., Mesa-Delgado A., López-Martín L., Esteban C., 2011, MNRAS, 411, 2076
Luridiana V., Morisset C., Shaw R. A., 2015, A&A, 573, A42
Marino R. A. et al., 2013, A&A, 559, A114
Masegosa J., Moles M., Campos-Aguilar A., 1994, ApJ, 420, 576
Matteucci F., 1986, MNRAS, 221, 911
Maza J., Ruiz M. T., Pena M., Gonzalez L. E., Wischnjewsky M., 1991, A&AS, 89, 389
Melnick J., Terlevich R., Terlevich E., 2000, MNRAS, 311, 629
Menacho V. et al., 2021, MNRAS, 506, 1777
Nagao T., Maiolino R., Marconi A., 2006, A&A, 459, 85
Newville M., Stensitzki T., Allen D. B., Ingargiola A., 2014, LMFIT: Non-Linear Least-Square Minimization and Curve-Fitting for Python. Zenodo
Olmo-García A., Sánchez Almeida J., Muñoz-Tuñón C., Filho M. E., Elmegreen B. G., Elmegreen D. M., Pérez-Montero E., Méndez-Abreu J., 2017, ApJ, 834, 181
Olofsson K., 1995, A&AS, 111, 57
Osterbrock D. E., 1989, S&T, 78, 491
Overzier R. A. et al., 2008, ApJ, 673, 143
Overzier R. A. et al., 2009, ApJ, 706, 203
Pagel B. E. J., Edmunds M. G., Fosbury R. A. E., Webster B. L., 1978, MNRAS, 184, 569

Pagel B. E. J., Edmunds M. G., Blackwell D. E., Chun M. S., Smith G., 1979, MNRAS, 189, 95

Pagel B. E. J., Simonson E. A., Terlevich R. J., Edmunds M. G., 1992, MNRAS, 255, 325

Papaderos P., Guseva N. G., Izotov Y. I., Noeske K. G., Thuan T. X., Fricke K. J., 2006, A&A, 457, 45

Pascual S., Cardiel N., Picazo-Sanchez P., Castillo-Morales A., de Paz A. G., 2019, guaix-ucm/megaradrp: v0.9.2

Pérez-Montero E., 2014, MNRAS, 441, 2663

Pérez-Montero E., Contini T., 2009, MNRAS, 398, 949

Pérez-Montero E., Díaz A. I., 2003, MNRAS, 346, 105

Pérez-Montero E., Díaz A. I., 2005, MNRAS, 361, 1063

Pérez-Montero E. et al., 2011, A&A, 532, A141

Pérez-Montero E., Kehrig C., Brinchmann J., Vílchez J. M., Kunth D., Durret F., 2013, Adv. Astron., 2013, 837392

Pérez-Montero E., Amorín R., Sánchez Almeida J., Vílchez J. M., García-Benito R., Kehrig C., 2021, MNRAS, 504, 1237

Pettini M., Pagel B. E. J., 2004, MNRAS, 348, L59

Pilyugin L. S., Vílchez J. M., Mattsson L., Thuan T. X., 2012, MNRAS, 421, 1624

Plionis M., Terlevich R., Basilakos S., Bresolin F., Terlevich E., Melnick J., Chavez R., 2011, MNRAS, 416, 2981

Porter R. L., Ferland G. J., Storey P. J., Detisch M. J., 2012, MNRAS, 425, L28

Porter R. L., Ferland G. J., Storey P. J., Detisch M. J., 2013, MNRAS, 433, L89

Raimann D., Storchi-Bergmann T., Bica E., Melnick J., Schmitt H., 2000, MNRAS, 316, 559

Rola C., Pelat D., 1994, A&A, 287, 676

Rosa-González D., Terlevich E., Terlevich R., 2002, MNRAS, 332, 283

Roy J. R., Kunth D., 1995, A&A, 294, 432

Ruan C.-Z., Melia F., Chen Y., Zhang T.-J., 2019, ApJ, 881, 137

Rynkun P., Gaigalas G., Jönsson P., 2019, A&A, 623, A155

Sánchez Almeida J., Muñoz-Tuñón C., Elmegreen D. M., Elmegreen B. G., Méndez-Abreu J., 2013, ApJ, 767, 74

Sánchez Almeida J., Morales-Luis A. B., Muñoz-Tuñón C., Elmegreen D. M., Elmegreen B. G., Méndez-Abreu J., 2014, ApJ, 783, 45

Sánchez Almeida J. et al., 2015, ApJ, 810, L15

Sargent W. L. W., 1970a, ApJ, 159, 765

Sargent W. L. W., 1970b, ApJ, 160, 405

Sargent W. L. W., Searle L., 1970, ApJ, 162, L155

Searle L., 1971, ApJ, 168, 327

Searle L., Sargent W. L. W., 1972, ApJ, 173, 25

Shields G. A., Searle L., 1978, ApJ, 222, 821

Storey P. J., Hummer D. G., 1995, MNRAS, 272, 41

Strom A. L., Steidel C. C., Rudie G. C., Trainor R. F., Pettini M., 2018, ApJ, 868, 117

Tayal S. S., 2011, ApJS, 195, 12

Tayal S. S., Zatsarinny O., 2010, ApJS, 188, 32

Telles E., 2003, in Perez E., Gonzalez Delgado R. M., Tenorio-Tagle G., eds, ASP Conf. Ser. Vol. 297, Star Formation Through Time. Astron. Soc. Pac., San Francisco, p. 143

Telles E., Melnick J., 2018, A&A, 615, A55

Telles E., Terlevich R., 1997, MNRAS, 286, 183

Telles E., Melnick J., Terlevich R., 1997, MNRAS, 288, 78

Tenorio-Tagle G., Munoz-Tunon C., Cid-Fernandes R., 1996, ApJ, 456, 264

Terlevich R., Melnick J., Masegosa J., Moles M., Copetti M. V. F., 1991, A&AS, 91, 285

Terlevich E., Diaz A. I., Terlevich R., Vargas M. L. G., 1993, MNRAS, 260, 3

Terlevich R., Terlevich E., Melnick J., Chávez R., Plionis M., Bresolin F., Basilakos S., 2015, MNRAS, 451, 3001

Thuan T. X., Pilyugin L. S., Zinchenko I. A., 2010, ApJ, 712, 1029

Tsiapi P. et al., 2021, MNRAS, 506, 5039

Valerdi M., Peimbert A., Peimbert M., Sixtos A., 2019, ApJ, 876, 98

Valerdi M., Barrera-Ballesteros J. K., Sánchez S. F., Espinosa-Ponce C., Carigi L., Mejía-Narváez A., 2021, MNRAS, 505, 5460

Vilchez J. M., Esteban C., 1996, MNRAS, 280, 720

Vílchez J. M., Iglesias-Páramo J., 2003, ApJS, 145, 225

Vincenzo F., Belfiore F., Maiolino R., Matteucci F., Ventura P., 2016, MNRAS, 458, 3466

Wofford A., Vidal-García A., Feltre A., Chevallard J., Charlot S., Stark D. P., Herenz E. C., Hayes M., 2021, MNRAS, 500, 2908

Wu Y., Cao S., Zhang J., Liu T., Liu Y., Geng S., Lian Y., 2020, ApJ, 888, 113

Wu Y.-Z., Zhang S.-N., 2013, MNRAS, 436, 934

Yennapureddy M. K., Melia F., 2017, J. Cosmology Astropart. Phys., 2017, 029

Zeippen C. J., 1982, MNRAS, 198, 111

SUPPORTING INFORMATION

Supplementary data are available at *MNRAS* online.

megarahii_metalicidad_revised_APPENDIX.pdf

Please note: Oxford University Press is not responsible for the content or functionality of any supporting materials supplied by the authors. Any queries (other than missing material) should be directed to the corresponding author for the article.

This paper has been typeset from a TeX/LaTeX file prepared by the author.